Analysis of Wideband Cylindrical Arrays

by

Peijun HAN

In partial fulfilment of the requirements for the degree of

MASTER OF SCIENCE

In

ELECTRICAL ENGINEERING

Supervisors:

Dr. D. Cavallo,
Ir. R. G. Tapia Barroso

July 1, 2025

Terahertz Sensing Group
Department of Microelectronics
Faculty of Electrical Engineering, Mathematics and Computer Science
Delft University Of Technology

TU Delft

To my family

Abstract

The demand for phased array antennas is expanding in modern society in both military and civil domains. Future applications will require the development of innovative antenna arrays with enhanced capabilities, e.g., wide/multi-band operation, wide scan range, multiple-beam radiation, and high polarization purity. In particular, broadband arrays have emerged as a prominent research focus in the field of phased array antennas due to their advantageous role in multifunctional antenna systems. In scenarios where space is limited, such as on complex platforms, there is a growing demand for ultra-wideband antenna apertures capable of supporting multiple functions.

Planar phased array antennas are typically designed on a flat, two-dimensional surface and are well-suited for applications where the antenna can be mounted on a flat platform. Their geometry simplifies both the design and fabrication processes, making them a common choice for ground-based radar systems, satellite communication panels, and base stations. However, their flat configuration can limit beam steering capabilities and may not conform well to the aerodynamic or structural constraints of more complex platforms. In contrast, conformal phased array antennas are designed to follow the shape of the surface they are integrated with, such as the curved fuselage of an aircraft. While conformal arrays offer these advantages, they also introduce greater design complexity, as the curvature affects the array behavior and necessitates more advanced modeling techniques.

This work aims to develop simulation methods to evaluate the performance of cylindrical arrays. First, the unit cell of the cylindrical array is investigated in terms of impedance and radiation properties, based on Ansys HFSS simulations with periodic boundary conditions. The results are compared with the benchmark of the planar array case for varying radii of curvature and different polarizations. The study also considers a connected slot element with multi-section anisotropic matching layers as an example of an ultra-wideband unit cell.

Subsequently, finite cylindrical arrays based on such a unit cell are studied in terms of edge effects and efficiency. The arrays are assumed to be finite along the cylinder curvature, but still periodic along the cylinder axis. A procedure is developed to calculate the optimal input phases of the array elements, to account for mutual coupling, impedance variation across the array, and anisotropy of the matching layers. Finally, some considerations on the comparison between cylindrical and planar array geometries are given.

Acknowledgements

This work was not undertaken alone; I received both technical and emotional support from many others.

First, my gratitude goes to my responsible supervisor, dr. Daniele Cavallo. Thank you, Daniele, for offering me the opportunity to work on this project and grow through learning and research. You guided me step by step as a newcomer to both coding and simulation tools, encouraging me to think more systematically and pay closer attention to detail. I am both humbled and impressed by your ability to uncover overlooked mistakes and propose novel approaches. Your thoughtful guidance, along with improvised puns and sense of rhythm, has influenced my own style of communication.

Also, I would like to thank my daily supervisor, Roderick Tapia Barroso who has a warm heart and entertaining laugh. While your provocative humor is always thrilling, your openness gives me the confidence to ask questions. I am especially grateful for your support with details, whether in hardware or software.

Likewise, thanks to all other professors and PhD students who spent their valuable time to help me better understand the concepts in the courses. All the help is greatly appreciated and I definitely feel like I've improved compared to where I started.

Thanks to the master students who were my classmates and office mates. Marick, the chaotic cool guy, you seem to take things as they come, but you are hardcore when something really grabs your interest. Pieter, every squad needs a Pieter, you speak with the cadence of a talk show host, yet back it up with a broad knowledge base, both within and beyond your field. Tom, the strict one, I truly admire your dedication to work and your passion for challenges. The fine dinner you hosted was memorable and thoughtful. Genuinely, thanks to all other colleagues for the lunch, coffees, drinks and birthday desserts. The environment created by the group is remarkable and it always inspires me to study and explore.

Thanks to my new nerdy and sporty friends in Delft, and to the online connection with my old friends elsewhere. Thank you to my parents for your full trust and I hope you enjoy your retirement. Many thanks to my aunt and uncle for their financial support. Your resilience and hard work have always encouraged me to face the adverse circumstance. To my cousins, whom I grew up with: I cherish the bond we have and I hope we can continue to stay connected and uphold our shared values.

This Page Intentionally Left Blank

Contents

1. Introduction

1.1 Wideband Wide-Scanning Phased Arrays

Antenna arrays capable of covering large bandwidths and scanning to large angles have received a lot of attention over the past decades. These properties find applications in different fields, both civil and military, e.g., satellite and base station communication [1–3], radio astronomy [4, 5], radar and electronic warfare [6, 7]. The attention to cover large bandwidths is the result of a trend to integrate multiple functionalities, operating in different frequency bands, on the same radiating aperture.

In the field of wideband, wide-scanning arrays, different antenna solutions have been proposed. A typical example is the tapered slot or Vivaldi antennas, which are capable of achieving a wide impedance matching bandwidth [8–10]. A drawback of Vivaldi arrays is the high level of cross-polarization, especially present for large scanning angles in the diagonal planes. A solution to this problem was recently proposed by resorting to sliced-notched Vivaldi elements [11, 12]. Nevertheless, these antennas are characterized by a relatively large height in terms of the wavelength, due to the long flare of the slots. Therefore, they are not suitable for low-profile designs. Moreover, the physical realization of this type of arrays makes use of vertically oriented printed circuit boards (PCBs), which often present challenges in terms of assembly and integration.

Another class of wideband arrays is that based on connected or tightly-coupled elements. These arrays can achieve a large impedance bandwidth as a result of strong coupling between elements. In this way, the strongly coupled elements approximate the ideal infinite current sheet introduced by Wheeler [13]. Many designs have been proposed based on this class of arrays, achieving a large impedance bandwidth, a low profile, and a large scan volume [14–17]. A successful implementation of connected array with state-of-the-art performance in terms of bandwidth, efficiency, and scan range is represented by connected slots loaded with Artificial Dielectric Layers (ADLs) [3, 18, 19]. They consist of an array of infinite slots, each excited at periodic locations. Both the slots and the feeds in each slot are spaced by about half a wavelength ($\lambda_0/2$) at the maximum frequency of operation. The electrical connection between slots results in a current distribution on the array that is nearly constant with frequency, thus achieving wideband properties. However, to obtain unidirectional radiation, it is necessary to introduce a backing reflector below the connected slot elements, which deteriorates the impedance matching performance of the array. To mitigate this effect, a wideband impedance transformer can be used, implemented by using ADLs above the slots. ADLs consist of periodically arranged subwavelength metallic square patches, which effectively provide an anisotropic response, thus allowing for a large scan volume as surface waves are not excited.

1.2 Conformal Arrays

Ultra-wideband antenna apertures can be especially advantageous for mobile platforms with size constraints that require multiple antennas for different functionalities, e.g., aircraft require different communication, radar and instrument antennas [20]. Typically, whenever high directivity is required for an antenna on these platforms, a large planar array capable of satisfying the requirements is designed and then mounted on the aircraft through an additional construction. This leads to deterioration of the aerodynamic performance of the aircraft. The integration of such a large array could benefit from a conformal antenna array.

The topic of conformal arrays began with the analysis of circular arrays, which were identified to have desirable properties for broadcasting, communications, navigation, and direction finding [20]. Through the correct phasing of the elements, a beam can be scanned over all azimuthal directions. In this context, cylindrical arrays have recently been used for polarimetric weather radars [21] and Unmanned Aerial Vehicle (UAV) detection [22], among other applications. The analysis and design of cylindrical arrays has been of interest for some time already [23–27], but remains a relevant research topic in more recent works [28], [29].

In this thesis, cylindrical connected slot arrays are investigated, with and without ADLs. To avoid computationally heavy simulations, the real ADLs comprising many small metallic patches are replaced by equivalent homogeneous anisotropic slabs, which are faster to simulate. Despite this simplification, the approximated structure with homogenized slabs still exhibits the same qualitative effects on the performance due to the array curvature.

1.3 Objectives of the Thesis

The goal of this work is to develop simulation methods to assess the performance of conformal arrays. First, we establish a benchmark by showing an example planar unit cell design based on connected slots. Then, the difficulties arising in simulating a cylindrical unit cell in Ansys High Frequency Structure Simulation Software (HFSS) are discussed, specifically related to the definition of perfectly matched layers as absorbing boundary. Once the cylindrical unit cell has been validated, we study how the input impedance of a cylindrical array converges to the equivalent planar array for different radii of curvature. In a realistic design, ADLs can be used to greatly improve the matching performance. However, when a large bandwidth is needed, the resulting ADLs superstrate will consist of many metallic layers. To analyze a 10:1 bandwidth connected array design, we reduce the simulation complexity by resorting to a simplified unit cell based on equivalent anisotropic slabs that mimic the ADLs behavior. The performance of both planar and cylindrical unit cells is compared.

Another objective of this work is to find the optimal input phases of a finite cylindrical array to maximize the directivity. In cylindrical arrays, the phase distribution should be such as to compensate for the curvature, so that a planar wavefront is achieved. It is relatively simple to calculate these phases for arrays radiating in free space with low mutual coupling. However, when mutual coupling, edge effects, and propagation in anisotropic slabs are taken into account, the required phases might differ significantly. For this reason, a technique that resorts to an analysis of reception is proposed. A plane wave illuminating a finite array structure is considered, where the phase is calculated at the equivalent feeding points of the array. Using the conjugate phases, the elements can be excited in transmission and a flat wavefront can be synthesized. Having derived a technique to compute the elements' phase excitation, a finite-by-infinite cylindrical array is studied and compared to its planar counterpart. The performance of the array is analyzed in terms of the matching efficiency for both broadside radiation and scanning configurations.

1.4 Thesis Outline

This work consists of the following chapters:

- Chapter 2 establishes a benchmark planar unit cell and then explains the method for simulating a cylindrical unit cell similar to the planar one. This chapter further studies the convergence of the input impedance as a function of the radius of curvature for both polarizations of a connected slot array. The procedure for obtaining the far-field from unit cell simulations is explained and validated.

- Chapter 3 focuses on the analysis of a wideband cylindrical unit cell. The cell consists of a connected slot element with anisotropic slabs above the slot to achieve ultra-wideband behavior. The anisotropic slabs have to be defined so that their axes of anisotropy are aligned with the normal vector at each element. The active input impedance is studied as a function of the radius of curvature.

- Chapter 4 explains the procedure for finding the phases of the elements in a finite cylindrical array, for connected arrays with or without anisotropic slabs. The latter case was achieved by using an equivalent simulation in reception in order to estimate the optimal phases.

- Chapter 5 studies the finiteness effects for conformal cylindrical arrays. A finite-by-infinite structure is simulated. The comparison is made with respect to the planar case considering the matching efficiency, directivity and gain, for broadside and for scanning in the plane along which the array is infinite.
- Chapter 6 provides the conclusion based on the study performed for cylindrical connected arrays. Interesting future research directions are identified and recommended.

This Page Intentionally Left Blank

2. Simulation Method for Cylindrical Arrays

This chapter describes the techniques used to simulate cylindrical connected slot arrays with the commercial software Ansys High Frequency Structure Simulation Software (HFSS) [30]. As is typically the case in planar arrays, we use a unit cell approach to simulate the array performance in terms of its active reflection coefficient and far-field patterns. The chapter focuses on clarifying difficulties that arise when curved arrays are considered in contrast to planar arrays.

2.1 The Unit Cell Approach

2.1.1 Planar Unit Cell Example

To estimate the performance of large planar arrays, the unit cell approach is typically used as it takes advantage of the periodic nature of the problem to reduce simulation complexity. Simulating the entire finite array with numerical methods is impractical for electrically large apertures, since the computational effort required to solve the problem increases with the number of elements. A different approach that can be employed is to approximate the finite array as an infinitely periodic array. In an infinite array environment, the analysis of the array reduces to the study of only one element (unit cell), which is repeated infinitely by assuming periodic boundary conditions (PBC). The solution of an infinitely periodic structure involves the so-called Floquet theorem [31]. It must be noted that this solution is an approximation: if we consider a finite array, the Floquet theorem solution will describe well the elements in the center of the array, but not the elements close to the edges of the array. Of course, the infinite array approximation is more accurate to describe large arrays. For small arrays, the edge effects resulting from the truncation must be taken into account to correctly assess the performance.

In order to study the performance of curved cylindrical arrays, we first establish a benchmark planar unit cell with which we will compare in the remainder of this thesis. The unit cell under analysis consists of a connected slot element, as depicted in Fig. 2.1. The slot has width w_s and is backed by a ground plane at a distance h_{br}. The period is assumed to be equal in the x- and y-directions, that is, $d_x = d_y$. Furthermore, conducting walls are used between the slot and ground plane to prevent the propagation of guided modes. The excitation consists of a delta-gap source with a defined width δ_s. All conductors are assumed to be Perfect Electrical Conductor (PEC).

The specific geometrical parameters of the planar unit cell analyzed in this section are reported in Table 2.1, where the parameters have been normalized to the wavelength λ_0 at the maximum considered frequency f_0. The unit cell can be built in HFSS, as shown in Fig. 2.2(a), where a lumped port (red rectangle in the figure) can be used as a feed. Furthermore, a vacuum block with height $h_{\mathrm{vacuuum}} = \lambda/4$ at the frequency $0.5f_0$ is placed above the slot (light blue in the figure). The top green box represents the Perfectly Matched layer (PML) defined as boundary on the top face of the vacuum, as seen in Fig. 2.2(b), which has the same size as the vacuum box $h_{\mathrm{PML}} = \lambda/4$. The PML is an anisotropic material that absorbs all electromagnetic energy, hence mimicking the radiation

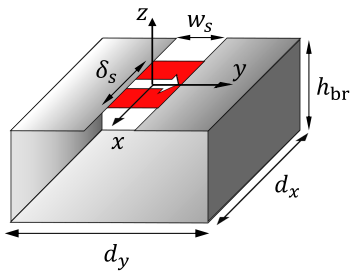

Figure 2.1: Schematic view of planar connected slot unit cell.

Table 2.1: Parameters of the planar connected slot array unit cell.

Description	Parameter	Value
Array period $\hat{x}$ direction	d_x	$0.4\lambda_0$
Array period $\hat{y}$ direction	d_y	$0.4\lambda_0$
Slot width	w_s	$0.13\lambda_0$
Feed length	δ_s	$0.2\lambda_0$
Back reflector distance	h_{br}	$0.2\lambda_0$

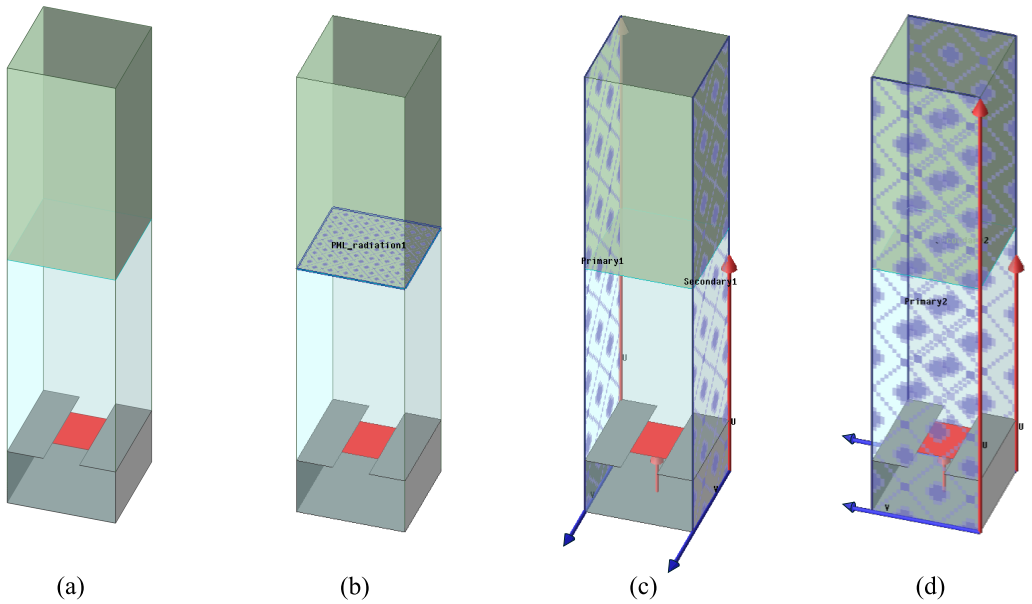

Figure 2.2: Unit cell model of a planar connected slot array in HFSS: (a) overview of the model, (b) PML boundary, (c) periodic boundary conditions in the E-plane, and (d) periodic boundary conditions in the H-plane.

condition. On the lateral sides of the unit cell, two lattice pair boundary conditions can be defined, as shown in Fig. 2.2(c) and (d), respectively, to enforce periodicity.

The active impedance of such an array can be simulated for different scanning conditions. The active impedance for broadside radiation is shown in Fig. 2.3(a), for scanning to 60° in the H-plane in Fig. 2.3(b) and in the E-plane in Fig. 2.3(c).

2.1.2 Cylindrical Unit Cells

In the case of the cylindrically connected slot array, due to the loss of symmetry, it is necessary to simulate two different single-polarized unit cells to study the different configurations of a possible dual-polarized array. One unit cell is curved along the E-plane, as shown schematically in Fig. 2.4(a), and one is curved along the H-plane, as in Fig. 2.4(b).

The specific geometrical parameters are defined in Table 2.2 and have been deliberately defined such that for a large radius of curvature, the unit cell converges to the planar case. This allows for a comparison between cylindrical and planar geometries as a function of the radius of curvature or the unit cell angle α.

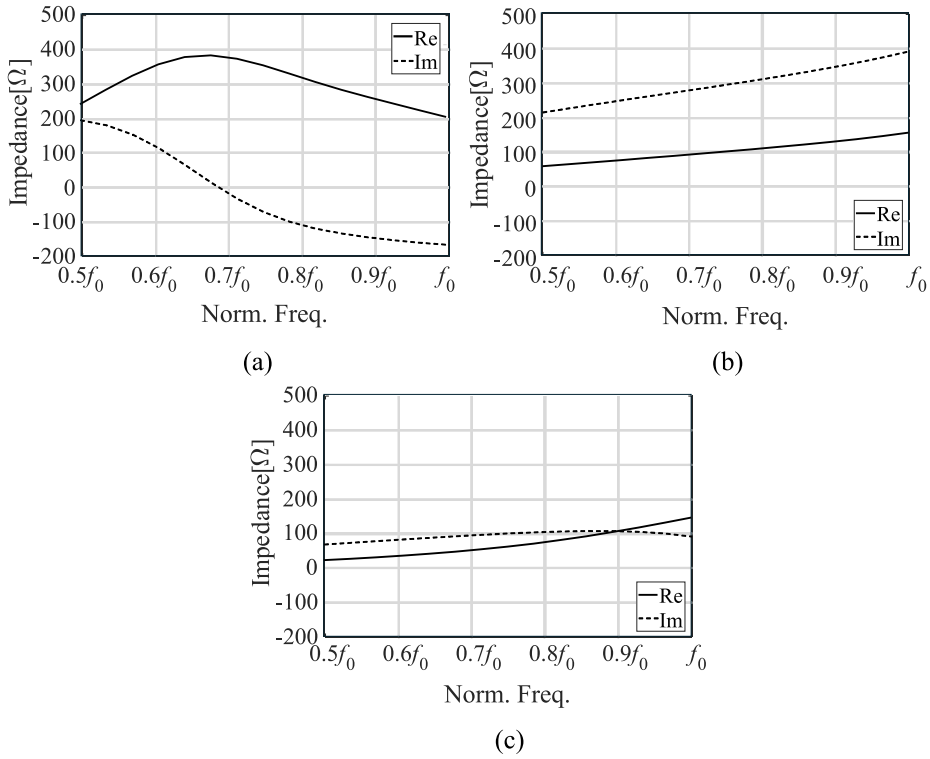

Figure 2.3: Active impedance of planar array unit cell for (a) broadside scanning, (b) scanning to 60° in the H-plane, and (c) scanning to 60° in the E-plane.

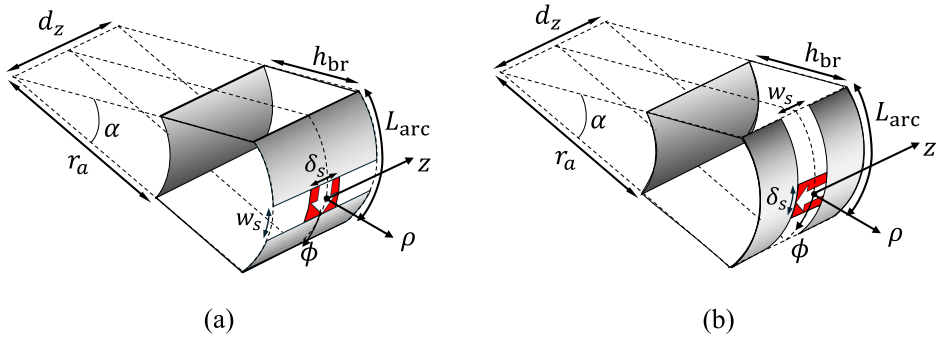

Figure 2.4: Unit cell schematic view of a cylindrical connected array, with the slots curved along (a) the E-plane and (b) the H-plane.

The implementation in HFSS is similar to the case of the planar array and can be seen in Fig. 2.5(a) and (b) for both polarizations, where the blue volume is made of vacuum and the green part represents the PML. In Fig. 2.5(b), the boundary conditions in the circumferential direction are shown, which are implemented as slanted planes, while Fig. 2.5(d) shows the periodic boundaries in the direction with no curvature.

The active impedance of a unit cell curved along the E-plane can be seen in Fig. 2.6. By using the default PML setup in HFSS, similarly to the planar case, the green curve of the active impedance is obtained. In addition to the characteristic resonance due to the ground plane, the impedance curve exhibits some unexpected fluctuations, likely due to the existence of unwanted reflections from

Table 2.2: Parameters of the cylindrical connected slot array unit cell.

Description	Parameter	Value
Number of unit cells in one ring	M	4 to 120
Array period $\hat{\phi}$ direction	α	$2\pi/M$
Array period $\hat{z}$ direction	d_z	$0.4\lambda_0$
Arc length of curved surface	L_{arc}	$0.4\lambda_0$
Slot width	w_s	$0.13\lambda_0$
Feed length	δ_s	$0.2\lambda_0$
Backing reflector distance	h_{br}	$0.2\lambda_0$
Radius	r_a	$L_{\text{arc}}/\alpha - h_{\text{br}}$

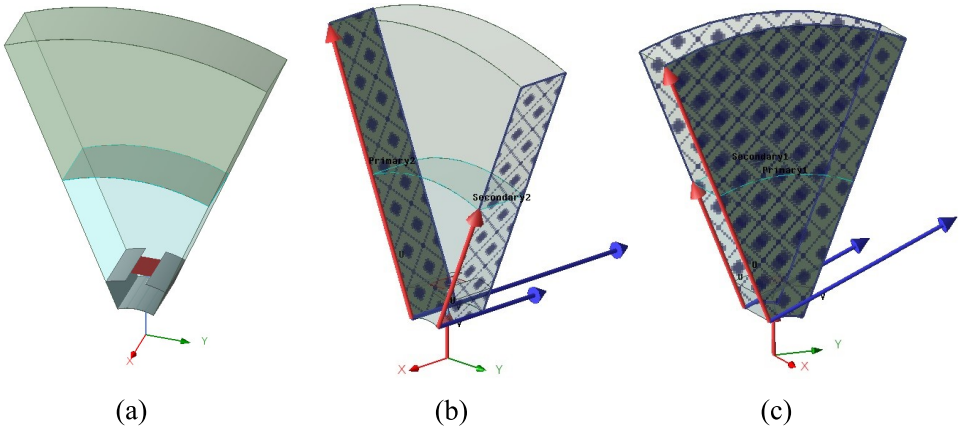

Figure 2.5: Unit cell model of a cylindrical connected slot array in HFSS: (a) curved unit cell with slot curved along the E-plane, (b) slanted periodic boundaries in the E-plane, and (c) parallel periodic boundaries in the H-plane.

the PML. These reflections can be explained by noting that the axes of anisotropy of the PML are defined according to the global Cartesian coordinate systems. Hence, the PML only absorbs well the electromagnetic field in the center of the unit cell, where the incidence is normal to the boundary. A possible solution to this problem is to divide the angular region of the unit cell into several smaller regions and define multiple PMLs. Each PML has the axes of anisotropy aligned with the local normal vector. This proposed solution results in a better estimation of the active impedance, as shown by the blue curve in Fig. 2.6, where the oscillations are no longer present.

Although the proposed approach is effective, it is time-consuming and impractical for the analysis of unit cells with varying radius of curvature. An alternative method is to use radiation boundaries (light blue curve in Fig. 2.6), which is simpler to implement, but still exhibits some discrepancy with respect to the split PML solution. Another method proposed in this work is to replace the PML with an absorber properly designed to dissipate the cylindrical wave that the array radiates, independently of the reference system. However, it should be noted that the proposed definition of the absorber boundaries can be used only for arrays that do not scan in the elevation plane. For scanning conditions, the split PML solution is still the most accurate one.

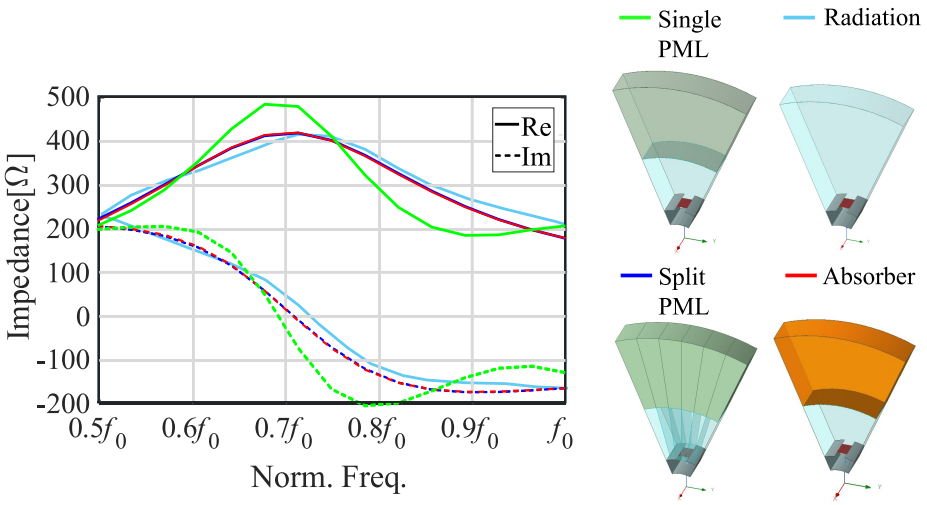

Figure 2.6: Active impedance of the cylindrical array unit cell for two different implementations of the PML, radiation and absorber boundary conditions.

2.1.3 Absorber Design

Instead of using the default PML boundary of HFSS, we define an absorber with the same goal of emulating the radiation condition. For this purpose, we define a lossy vacuum-like dielectric with the following additional properties

$$\tau_e = \tau_m = 1 \tag{2.1}$$

$$L = \frac{\lambda_{\max}}{2} \tag{2.2}$$

where τ_e is the dielectric loss tangent, τ_m is the magnetic loss tangent, and L is the thickness of the absorber in the radial direction. $\lambda_{\max}$ is the wavelength at the lowest frequency of analysis.

To explain the operation of the absorber, we note the HFSS assumes PEC by default at any interface where no boundary is defined. Therefore, the propagation in the absorber for normal incidence can be represented as an equivalent transmission line terminated with a short circuit, as shown in the inset of Fig. 2.7. The characteristic impedance, the wavenumber, and the active impedance of the absorber can be calculated as

$$\eta_{\text{vacuum}} = \sqrt{\frac{\mu_0}{\epsilon_0}} = \eta_0 \tag{2.3}$$

$$\eta_{\text{absorber}} = \sqrt{\frac{\mu}{\epsilon}} = \frac{\sqrt{\mu_0(1-j\tau_m)}}{\sqrt{\epsilon_0(1-j\tau_e)}} = \eta_0 \tag{2.4}$$

$$k_{\text{absorber}} = \omega\sqrt{\mu\epsilon} = \frac{2\pi}{\lambda}(1-j) \tag{2.5}$$

$$Z_{\text{in}} = j\eta_{\text{absorber}} \tan(k_{\text{absorber}} L) = j\eta_0 \tan\left(2\pi(1-j)\frac{L}{\lambda}\right). \tag{2.6}$$

The active impedance Z_{in}, normalized to the vacuum impedance, is plotted in Fig. 2.7 as a function of the absorber thickness L. It can be observed that for $L > \lambda/2$, the impedance is matched and no reflection occurs. Thus, the absorber must be at least $\lambda_{\max}/2$ thick.

Intuitively, the slanted periodic boundaries will replicate the curved unit cell in the same plane to form a ring structure with a certain radius r_a. The parallel periodic boundary conditions linearly

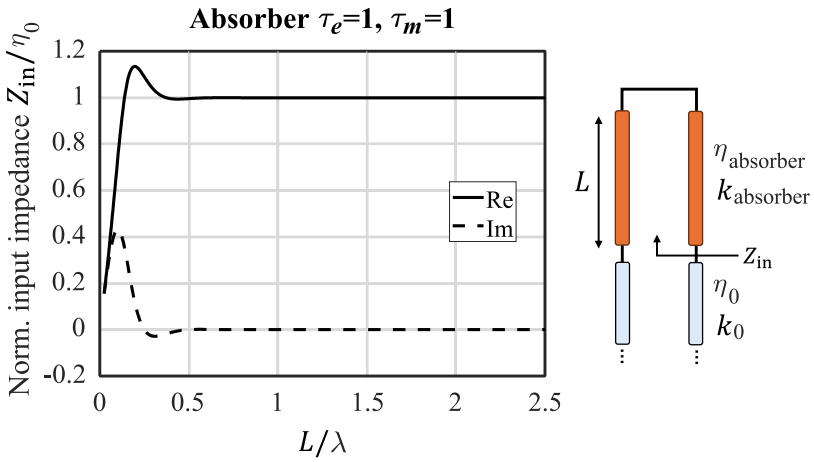

Figure 2.7: Input impedance of the proposed absorber normalized to the free space impedance, as a function of the absorber thickness in terms of the wavelength.

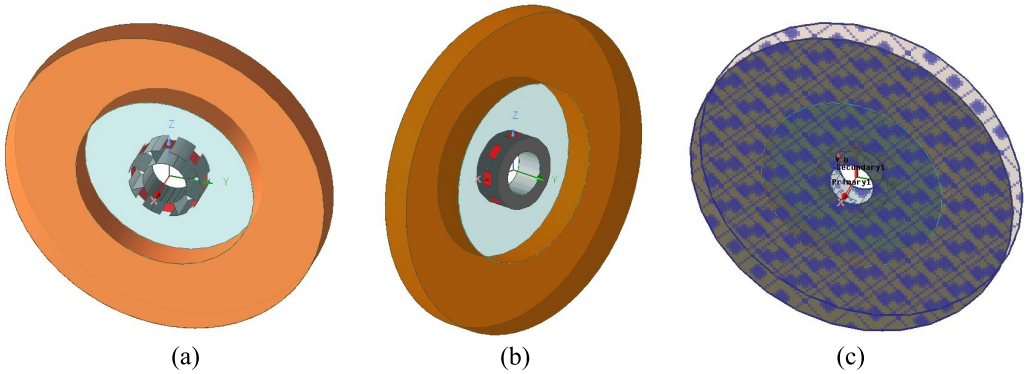

Figure 2.8: Complete ring of the connected slot array in HFSS: (a) array curved along the E-plane and (b) along the H-plane, and (c) periodic boundaries along the cylinder axis.

replicate the ring structure to form an infinitely long cylindrical array. To verify that this pair of slanted boundaries work as expected, the corresponding complete ring slot array is built and simulated in both HFSS and CST Studio Suite (CST) [32], as shown in Fig. 2.8 and Fig. 2.9, respectively. The parameter α is set as a relatively large ($\alpha = \pi/4$) so that the corresponding ring array is relatively small (8 elements along the circumference) and can be simulated with low computational effort. Each port in the complete ring simulation is excited with the same magnitude and phase, so that the active impedance of each port is expected to be the same due to symmetry. In addition, periodic boundaries are applied only in the direction along the cylinder axis, for both HFSS [see Fig. 2.8(c)] and CST [see Fig. 2.9(c)].

In Fig. 2.10, the active input impedance calculated with the unit cell approach is compared with the complete ring approach, for both the cases of the array curved in the E-plane and in the H-plane. The active impedance is the same for all elements in the complete ring simulation due to rotational symmetry. The real and imaginary parts of the active impedance are in good agreement for the two approaches in HFSS, as illustrated in Fig. 2.10(a) and Fig. 2.10(b). Despite some discrepancies, the CST simulation of the full ring also shows similar impedance curves to HFSS. In summary, the unit cell simulations are validated by comparison with the complete ring simulations and will be used in the remainder of this thesis to study the impedance properties of cylindrical arrays.

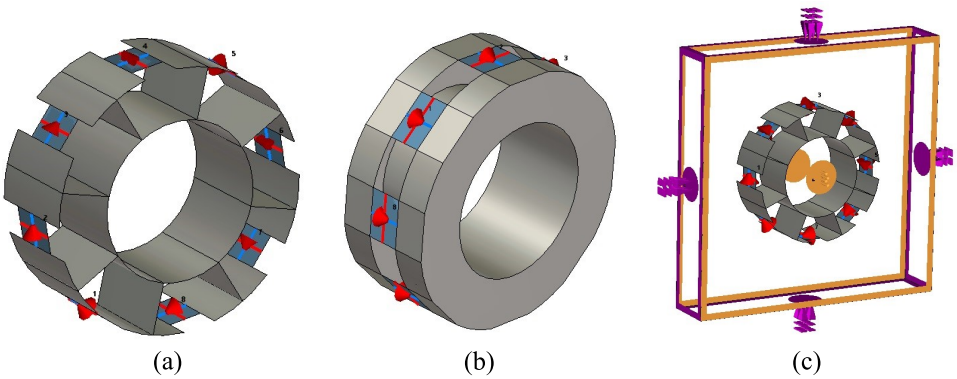

Figure 2.9: Complete ring of the connected slot array in CST: (a) array curved along the E-plane and (b) along the H-plane, and (c) periodic boundaries along the cylinder axis.

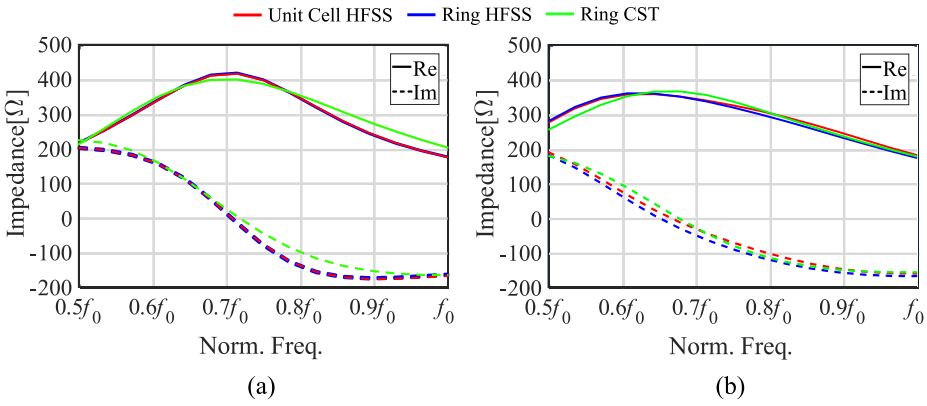

Figure 2.10: Active impedance of cylindrical array with (a) slots curved along the E-plane and (b) along the H-plane: comparison between unit cell approach in HFSS and a complete ring in both HFSS and CST.

2.2 Active Impedance Convergence of the Cylindrical Array

Cylindrical arrays with a small radius of curvature exhibit a different input impedance with respect to the planar array, as can be seen by comparing Fig. 2.10 ($M = 8$, $\alpha = \pi/4$) with Fig. 2.3(a).

To better highlight this behavior, Fig. 2.11 reports the active input impedance of the cylindrical unit cells, curved along the E- and the H-plane, for different radii of curvature. The parameter M, which indicates the number of elements in a ring, varies from 4 (corresponding to $\alpha = \pi/2$) to 120 (corresponding to $\alpha = \pi/60$). It can be noted in Fig. 2.11(a) that the impedance of small cylindrical arrays curved along the E-plane is significantly different from that of the planar array. For example, the curve for $M = 4$ is shifted to a higher frequency and gives a higher maximum value of input resistance. However, for larger values of M, the impedance curves converge to the planar array case. Faster convergence with M is observed for the array curved along the H-plane, shown in Fig. 2.11(b). Since the mutual coupling between the array elements is usually stronger in the E-plane [33, Figure 13(b)], the active impedance of the cylindrical array is more affected by the curvature in the E-plane.

In general, the convergence of the impedance properties of the cylindrical array to the limit of the planar array is already achieved for small arrays ($M = 16$). However, the considered unit cell is not wideband, thus the radius of curvature is still comparable to the wavelength at the lowest of investigation. The same study will be conducted for ultra-wideband unit cells over much larger

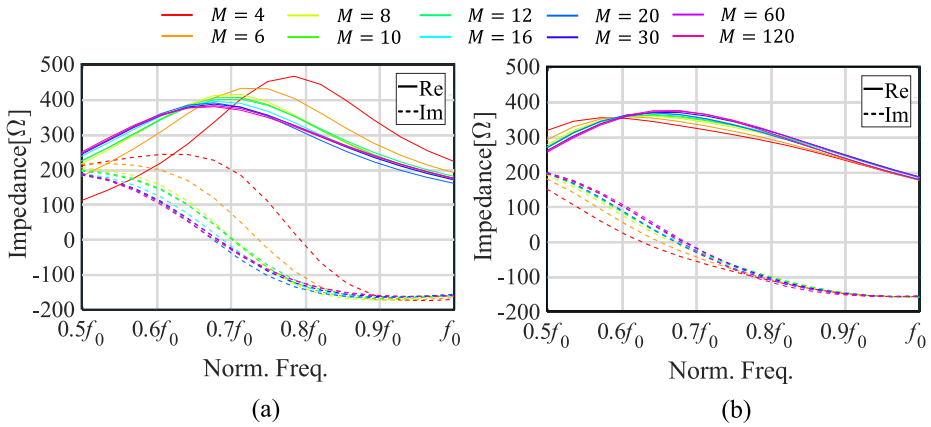

Figure 2.11: Active impedance of cylindrical array for different radii of curvature with (a) slot curved along the E-plane and (b) along the H-plane.

frequency ranges in Chapter 3.

2.3 Far-Field Patterns of the Cylindrical Array

2.3.1 Array Factor

The cylindrical array consists of a configuration of antenna elements arranged periodically in a two-dimensional pattern that wraps around a cylinder. In a planar array, the elements are typically arranged in a rectangular grid (x and y directions), as shown in Fig. 2.12(a). In contrast, the elements of a cylindrical array are placed around the curved surface (azimuthal ϕ direction) and along the z axis, as illustrated in Fig. 2.12(b).

The total radiation pattern of a phased array depends on the pattern of the individual antenna elements and their position in the array. The latter is closely related to the array factor, which is defined as a complex-valued far-field radiation pattern of the array, assuming the elements to be isotropic radiators. Let us assume the general case of an array composed of N isotropic antenna elements whose positions are indicated by the vectors $\vec{r}_n$. The intensity of the electric field radiated by this array at the point $\vec{r} = (r, \theta, \phi)$ can be expressed as

$$|\vec{E}(\vec{r})| \propto \sum_{n=1}^{N} I_n \frac{e^{-jk|\vec{r}-\vec{r}_n|}}{|\vec{r}-\vec{r}_n|} \tag{2.7}$$

where I_n is the complex excitation of the n-th antenna and k is the wavenumber. Approximations can be made to obtain a simplified form that is valid in the far-field region: for the amplitude of the field, the distance of the observation point $\vec{r}$ to each element of the array is assumed to be approximately equal, i.e. $|\vec{r}| \approx |\vec{r}-\vec{r}_n|$ for each n. For the phase of the field, the relative distance compared to the wavelength matters, so the same approximation made for the amplitude is not accurate. Therefore, a better approximation for the phase term can be assumed as $|\vec{r}-\vec{r}_n| \approx |\vec{r}| - \hat{k}\cdot\vec{r}_n$, where $\hat{k} = \vec{k}/k$ and $\vec{k}$ is the propagation vector:

$$\vec{k} = k\sin\theta\cos\phi\,\hat{x} + k\sin\theta\sin\phi\,\hat{y} + k\cos\theta\,\hat{z}\,. \tag{2.8}$$

By applying the two mentioned approximations, the array factor can be defined as the following

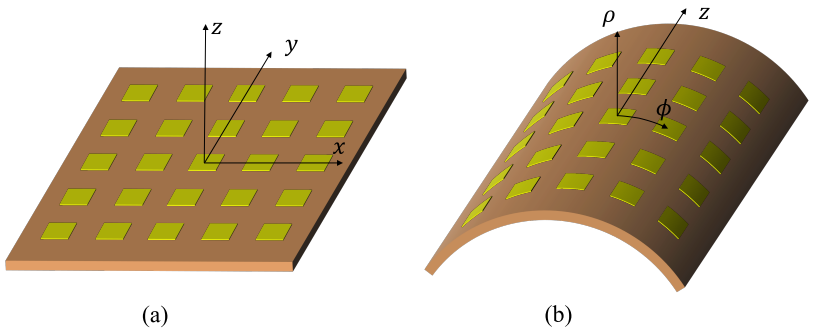

Figure 2.12: Schematic view of (a) a planar array and (b) a cylindrical array, with their coordinates systems.

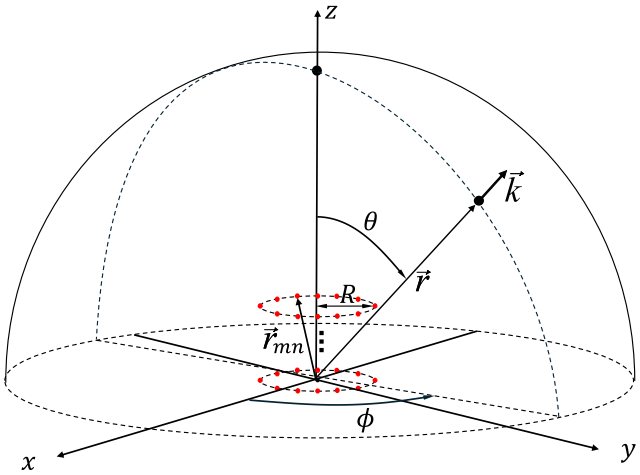

Figure 2.13: Cylindrical array geometry with reference coordinate system.

expression:

$$AF = \sum_{n=1}^{N} I_n e^{j\vec{k}\cdot\vec{r}_n} \tag{2.9}$$

Let us now consider the specific case of a cylindrical array made of N rings along z spaced by d_z, with each ring containing M elements, as shown in Fig. 2.13. The position of the element with indexes m along the ring and n along z is indicated as $\vec{r}_{mn}$:

$$\vec{r}_{mn} = R\cos m\alpha\,\hat{x} + R\sin m\alpha\,\hat{y} + nd_z\,\hat{z}. \tag{2.10}$$

where R is the radius of the ring. The array factor becomes

$$AF = \sum_{n=0}^{N-1}\sum_{m=0}^{M-1} e^{jkR\sin\theta\cos(\phi-m\alpha)+jknd_z\cos\theta}. \tag{2.11}$$

2.3.2 Array Pattern from Unit Cell Simulations

A method for constructing the array pattern from the unit cell simulation is described in Appendix A and is used here to report the radiation patterns of the connected slot array. The expression of the array factor in (2.11) is used in combination with the element patterns, which are azimuthally rotated replicas of the unit cell simulated pattern. For example, Fig. 2.14 shows the pattern of the

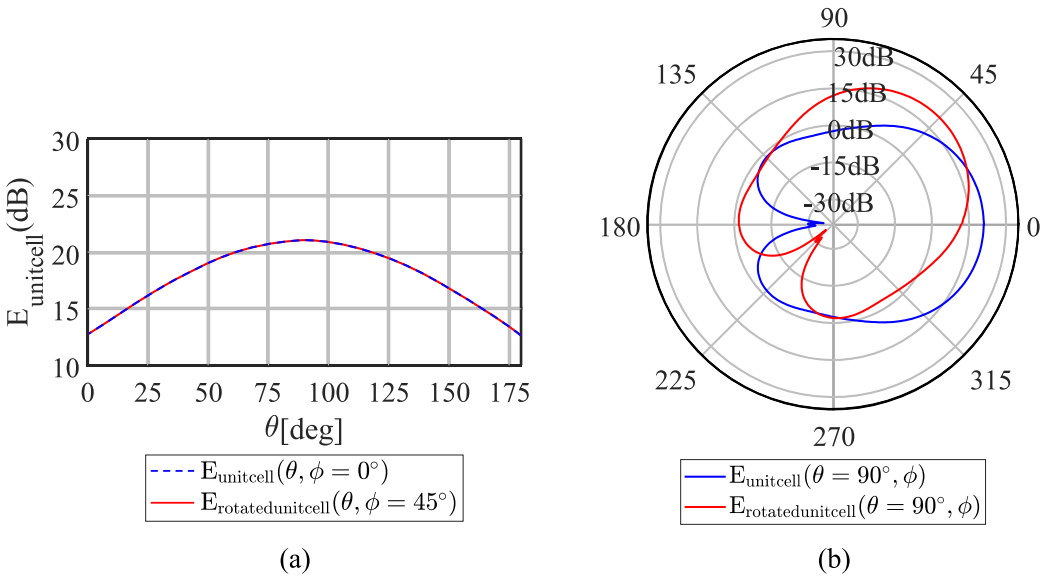

Figure 2.14: Radiation patterns cuts of unit cells before and after rotation by α in the (a) elevation and (b) azimuth planes.

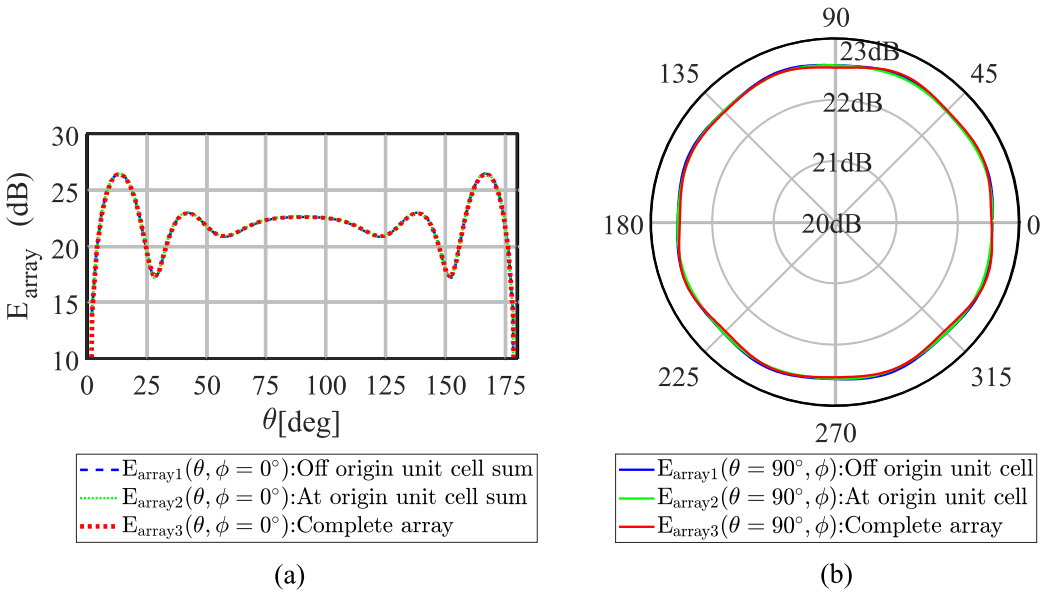

Figure 2.15: Radiation patterns cuts of cylindrical array calculated from unit cell and complete ring simulations in the (a) elevation plane and (b) azimuth plane.

connected slot unit cell, curved along the E-plane, with $M = 8$ and dimensions as in Table 2.2. The pattern is reported in the elevation plane $\phi = 0°$ and in the azimuth plane $\theta = 90°$. The pattern of another element, obtained by post-processing through azimuthal rotation by $\alpha = 45°$, is also shown in the figure.

The radius of the array for the connected slot unit cell is given by $R = r_a + h_{\mathrm{br}}$. The pattern of the array can be found with the procedure described in Appendix A, which starts from the pattern of a single unit cell and considers a shift in ϕ and a rotation of the field to find the patterns of all

the other unit cells. Two possibilities for the choice of the reference systems are considered, one with the origin at the element feed and one with the origin at the center of the cylinder. These two choices result in different definitions of the array factor. The resulting pattern is reported in Fig. 2.15(a) for the elevation plane $\phi = 0^\circ$ and in Fig. 2.15(b) for the azimuth plane $\theta = 90^\circ$. To validate the procedure, we show that both choices of the reference system as well as the complete array simulation provide the same results.

It can be noted that the pattern in the azimuth plane is omnidirectional, since the elements have the same phase and radiate maximally in the radial direction. If the embedded element pattern becomes more directive, for example, by adding artificial dielectric layers to achieve wide bandwidth, some oscillations can occur in the pattern. Moreover, the oscillations are frequency dependent and typically increase at the high end of the operational band. Thus, it is relevant to apply the methods presented in this chapter to an ultra-wideband connected array unit cell.

This Page Intentionally Left Blank

3. Unit Cell Analysis of Ultra-wideband Cylindrical Array

Since the objective of this work is the analysis of cylindrical ultra-wideband arrays, we introduce in this chapter a wideband connected array unit cell. This element will be used for the analysis of the cylindrical array geometry.

An established method to improve the bandwidth of a connected array is to place artificial dielectric layers (ADLs) above the slots [3, 18, 19]. The ADLs consist of multiple capacitive meshes made of periodic sub-wavelength patches, to implement a wideband impedance transformer. The ADLs are equivalent to an effective anisotropic medium whose permittivity and permeability tensors can be controlled by the spatial arrangement of the patches. The anisotropy gives the benefit of a large scanning capability with no surface waves. However, to avoid long simulations that would be required by meshing all patches, we replace the ADLs with equivalent anisotropic homogeneous slabs, which can be simulated in a fraction of the time.

3.1 Equivalent Homogeneous Anisotropic Slabs

A slab made up of one or more ADLs can be homogenized following the procedure described in [34]. Knowing the reflection and transmission coefficients of a plane wave impinging on the slab, for both transverse electric (TE) and transverse magnetic (TM) incidence, and for normal and oblique incidence, the effective permittivity and permeability tensors can be retrieved. The schematic side view of the ADLs and its equivalent homogeneous dielectric slab are shown in Fig. 3.1(a) and (b), respectively.

For ADLs made of square patches in vacuum ($\varepsilon_{\text{host}} = 1$), periodic along x and y, and stacked along z, the equivalent anisotropic tensors are defined as follows:

$$\bar{\bar{\varepsilon}} = \begin{bmatrix} \varepsilon_{xx} & 0 & 0 \\ 0 & \varepsilon_{yy} & 0 \\ 0 & 0 & \varepsilon_{zz} \end{bmatrix}, \quad \bar{\bar{\mu}} = \begin{bmatrix} \mu_{xx} & 0 & 0 \\ 0 & \mu_{yy} & 0 \\ 0 & 0 & \mu_{zz} \end{bmatrix}.$$

The effective refractive index for transverse electric (TE) and transverse magnetic (TM) waves can be obtained as [35]:

$$n_{\text{TM}} = \sqrt{\varepsilon_x \mu_y + (1 - \varepsilon_x/\varepsilon_z)\sin^2\theta} \tag{3.1}$$

$$n_{\text{TE}} = \sqrt{\varepsilon_y \mu_x + (1 - \mu_x/\mu_z)\sin^2\theta}\,. \tag{3.2}$$

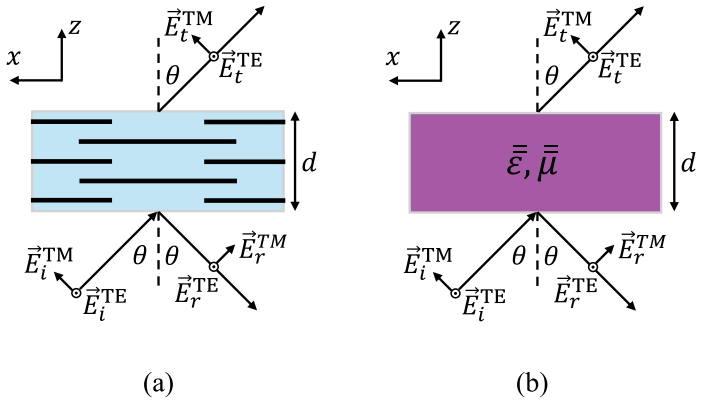

Figure 3.1: (a) A slab of ADLs and (b) its homogeneous equivalent anisotropic dielectric slab.

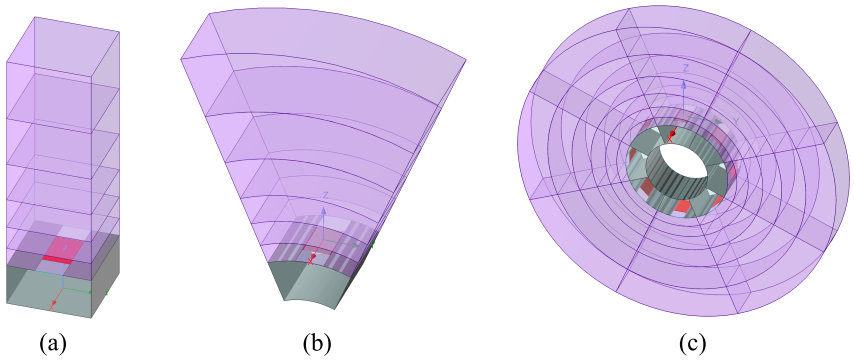

Figure 3.2: (a) Ultra-wideband planar connected slot unit cell with anisotropic slabs, (b) correspondent cylindrical unit cell and (c) its equivalent complete cylindrical array in HFSS.

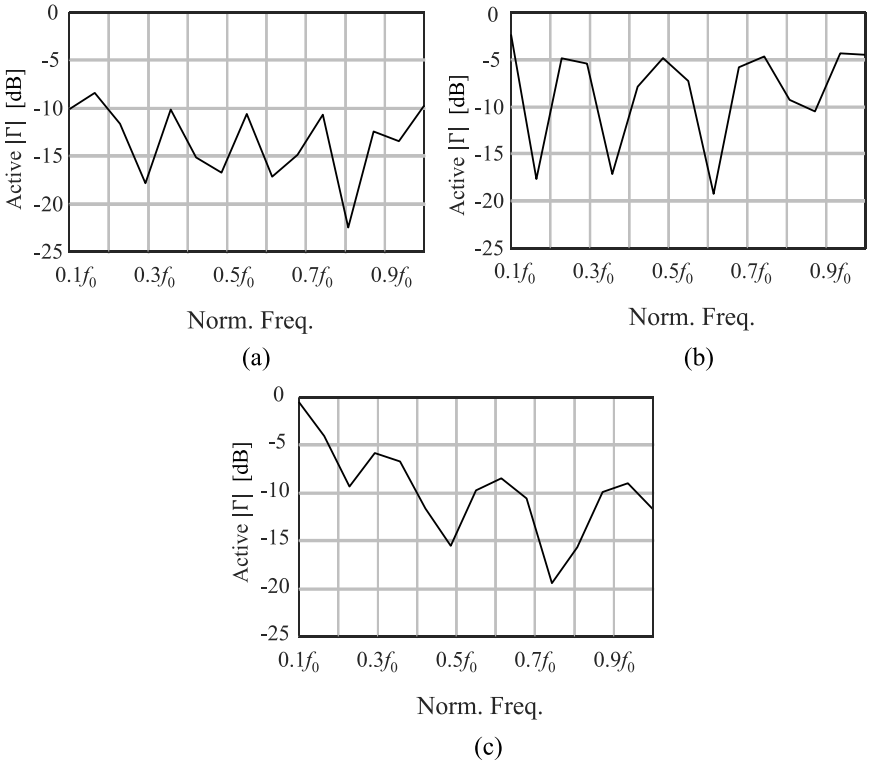

Figure 3.3: Active reflection coefficient of the ultra-wideband planar array for (a) broadside radiation, (b) scanning to 60° in the H-plane, and (c) scanning to 60° in the E-plane.

The matrices in (3.1) are diagonal, which means there is no coupling between the TE and TM modes. That is, the slab can only scatter TE waves under TE plane-wave incidence and can only scatter TM waves under TM plane-wave incidence. In addition, the equivalent dielectric slab maintains the property of ADLs, where $\varepsilon_{xx} = \varepsilon_{yy}, \varepsilon_{zz} = \varepsilon_{\text{host}} = 1$ and $\mu_{xx} = \mu_{yy}, \mu_{zz} < 1$ [35].

Table 3.1: xx-component of the permitivity tensor and thickness of the dielectric slabs.

Slab index (from bottom to top)	1	2	3	4	5	6
ε_{xx}	25	16	9.8	5.8	3.5	2.3
Thickness $h_{\text{dielectric}}$	$0.05\lambda_c$	$0.0625\lambda_c$	$0.08\lambda_c$	$0.105\lambda_c$	$0.135\lambda_c$	$0.165\lambda_c$

3.1.1 Ultra-wideband Planar Array

A ultra-wideband unit cell with 10:1 bandwidth ($0.1f_0$ to f_0) can be obtained with six slabs of ADLs that implement a multiple quarter-wave impedance transformer. The resulting unit cell is built in HFSS using equivalent anisotropic slabs, as shown in Fig. 3.2(a). The 6 anisotropic slabs implement a Chebyshev impedance transformer from 377Ω to 50Ω [36]. The specific values of the anisotropic tensors are reported in Table 3.1 for the xx-component of the permittivity. The thickness of the slabs is also reported in terms of the wavelength λ_c at the center frequency in vacuum, calculated according to $h_{\text{dielectric}} = \lambda_c/4/\sqrt{\varepsilon_{xx}}$. The dimensions of the slot elements are the same as specified in Table 2.1.

The simulation results of this unit cell are shown in Fig. 3.3 and Fig. 3.4. Fig. 3.3 reports the active reflection coefficient for broadside and scanning to 60° in the E- and H-plane. The broadside active reflection coefficient shows values mostly below −10 dB over the entire band of interest $[0.1f_0, f_0]$. However, the matching degrades when the array scans to large angles in both the E- and H-plane. In typical designs, an additional matching network comprising a series capacitor is included in the feeding structure to improve the matching when scanning [19]. However, for the study reported in this chapter, this series capacitor is not considered, since the focus is more on the comparison between cylindrical and planar arrays. The active input impedance of the unit cell is also shown in Fig. 3.4, for the three scanning configurations considered.

3.1.2 Ultra-wideband Cylindrical Array

A cylindrical unit cell, constructed from the planar geometry, is depicted in Fig. 3.2(b). The unit cell is obtained by tilting two of the walls by an angle α and maintaining the arc at the slot plane equal to the period of the planar case. The resulting geometrical parameters are the same as those given in Table 2.2. To assess the accuracy of the unit cell simulation, we compare it with a simulation of the complete cylindrical array ring, as shown in Fig. 3.2(c).

In the planar connected slot array, the axes of anisotropy of the slabs are the same for all the elements and aligned with the axes of the global coordinate system. In contrast, in the cylindrical array, every element has a different normal direction to the anisotropic slab stratification. For this reason, the definition of the permittivity and permeability tensors changes for each element.

To account for this aspect, two different approaches have been used. The first consists in defining the slabs for each element according to the global reference system, but rotated by a multiple of the angle α, as shown in Fig. 3.5(a). The second approach, which gives the same result, consists of defining the slabs of each element according to a local reference system aligned with the local normal direction, so that the same tensor definitions can be used for all elements [see Fig. 3.5(b)].

In the first approach, the rotated tensors can be calculated as follows

$$\overline{\overline{\varepsilon'}} = \mathbf{R}_x^T(\gamma)\bar{\bar{\varepsilon}}\mathbf{R}_x(\gamma) = \begin{bmatrix} \varepsilon_{xx} & 0 & 0 \\ 0 & \varepsilon_{yy}\cos^2\gamma + \varepsilon_{zz}\sin^2\gamma & -\varepsilon_{yy}\cos\gamma\sin\gamma + \varepsilon_{zz}\cos\gamma\sin\gamma \\ 0 & -\varepsilon_{yy}\cos\gamma\sin\gamma + \varepsilon_{zz}\cos\gamma\sin\gamma & \varepsilon_{yy}\sin^2\gamma + \varepsilon_{zz}\cos^2\gamma \end{bmatrix} \tag{3.3}$$

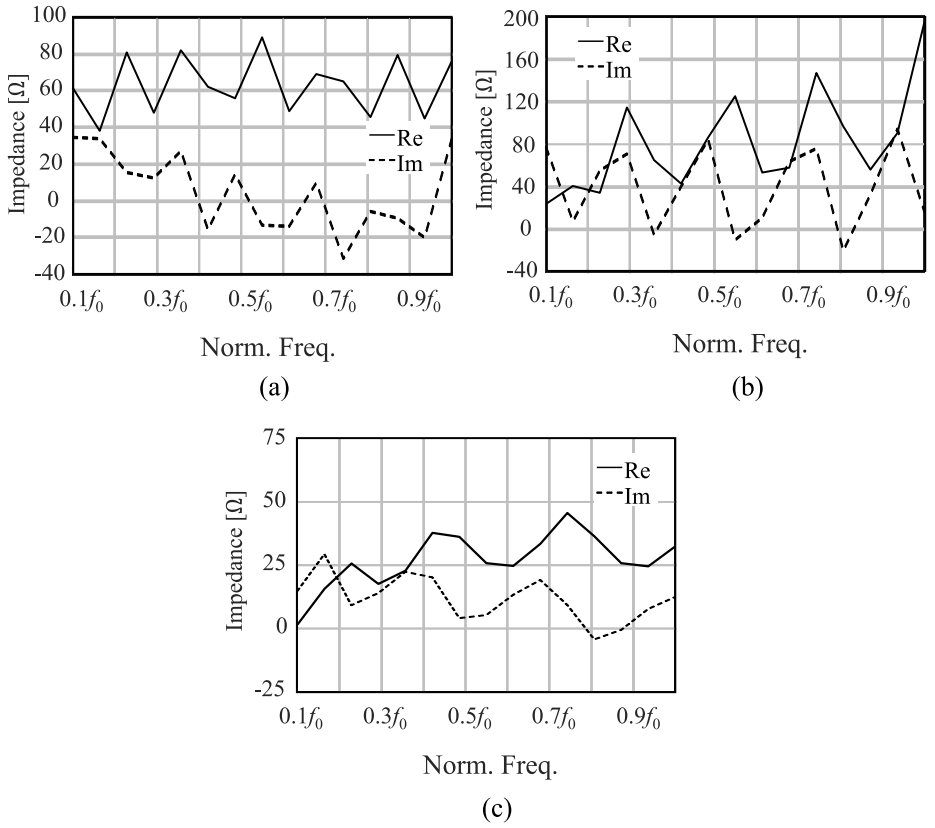

Figure 3.4: Active input impedance of the ultra-wideband planar array for (a) broadside radiation, (b) scanning to 60° in the H-plane, and (c) scanning to 60° in the E-plane.

where the rotation matrix with respect to the x-axis is defined as

$$\mathbf{R}_x(\gamma) = \begin{bmatrix} 1 & 0 & 0 \\ 0 & \cos\gamma & -\sin\gamma \\ 0 & \sin\gamma & \cos\gamma \end{bmatrix} \tag{3.4}$$

and $\gamma = m\alpha$. In general, the rotation for the two tensors, clockwise or counterclockwise, can be derived as in Table 3.2. Clockwise and counterclockwise rotations are defined when the axis about which they occur points toward the observer.

Table 3.2: Rotated anisotropic tensor under global coordinates

Direction	Permittivity	Permeability
Clockwise	$\bar{\bar{\varepsilon}}' = \mathbf{R}^T\bar{\bar{\varepsilon}}\mathbf{R}$	$\bar{\bar{\mu}}' = \mathbf{R}^T\bar{\bar{\mu}}\mathbf{R}$
Counterclockwise	$\bar{\bar{\varepsilon}}' = \mathbf{R}\bar{\bar{\varepsilon}}\mathbf{R}^T$	$\bar{\bar{\mu}}' = \mathbf{R}\bar{\bar{\mu}}\mathbf{R}^T$

The active input impedance of the ultra-wideband unit cell approach and the complete ring approach is shown in Fig. 3.6. α is still set as a relatively large angle ($\alpha = \frac{\pi}{4}$) so the corresponding array is relatively small ($M = 8$) and can be simulated efficiently. Six cylindrical anisotropic slabs, with the same tensors $\bar{\bar{\varepsilon}}, \bar{\bar{\mu}}$ and thickness as the planar case, are considered. The absorber (orange

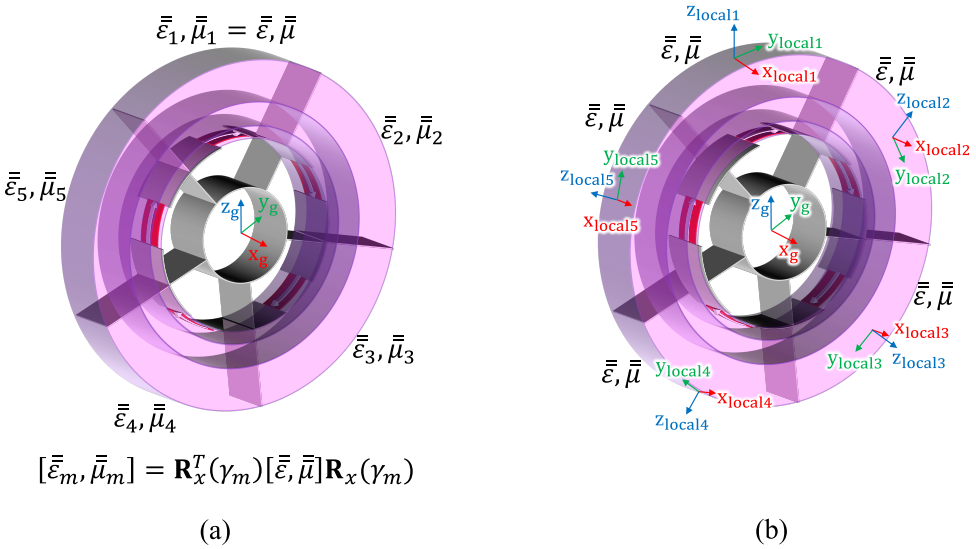

Figure 3.5: Cylindrical connected slot arrays loaded with anisotropic dielectric slabs: (a) tensor rotation with respect to single global reference system and (b) definition of local coordinate system for each unit cell.

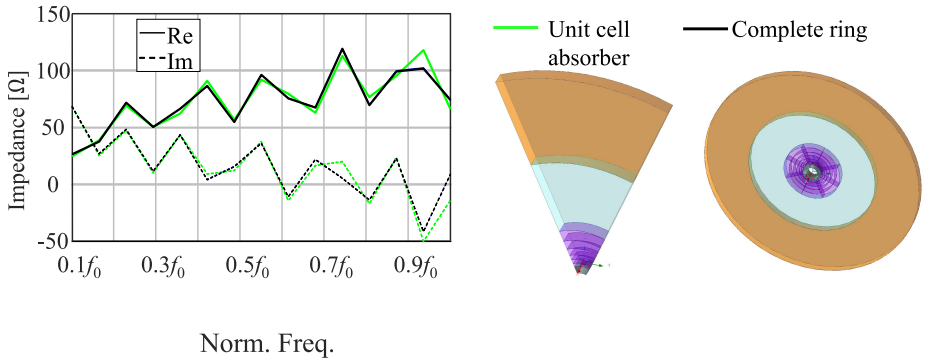

Figure 3.6: Active impedance of ultra-wideband cylindrical array: comparison between unit cell and complete ring simulations.

volume in the inset of Fig. 3.6) has a thickness of $\lambda/2$ at the lowest frequency $0.1f_0$. The complete ring array has also been simulated, with both the rotated tensor approach and the definition of the local coordinate systems. The active impedance of both the unit cell and the complete ring array shows good agreement. The unit-cell method is then used for the convergence study of the active impedance of the ultra-wideband cylindrical array versus the radius of curvature.

3.2 Active Impedance Convergence of Wideband Cylindrical Array

A parametric analysis by sweeping the number of elements M (related to the radius of curvature) is carried out for the wideband cylindrical unit cell, for slots curved in both the E- and H-plane. As expected, the simulation results show that the active impedance and reflection coefficient converge to the wideband planar array for larger and larger M, as seen in Fig. 3.7.

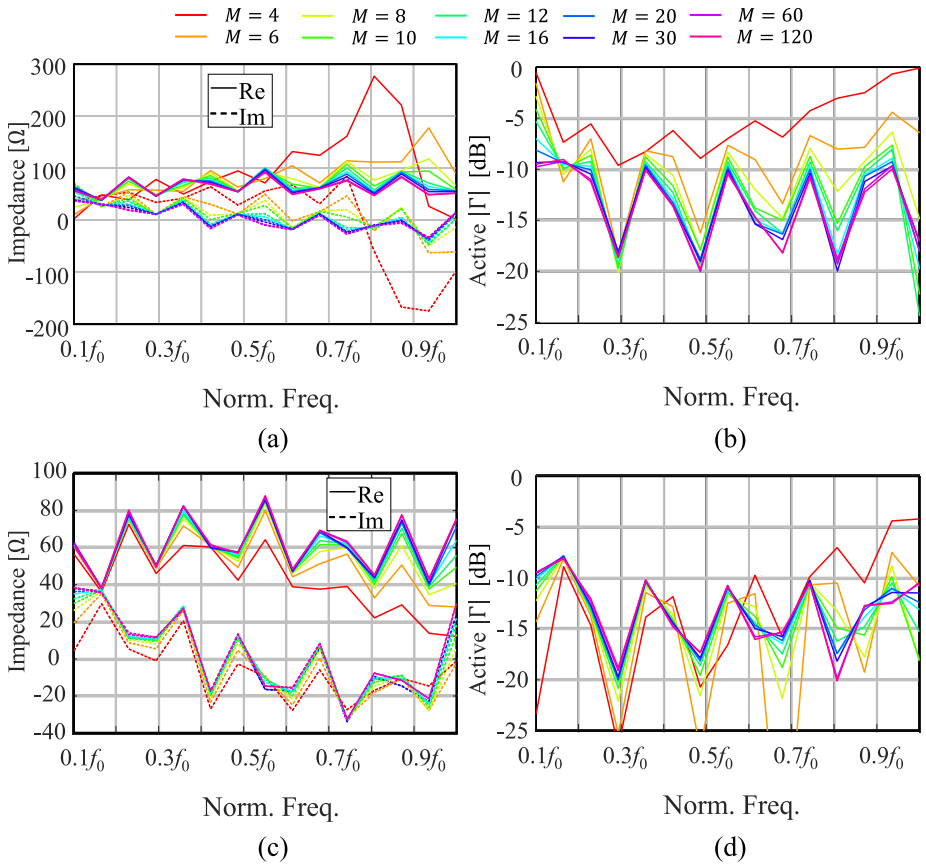

Figure 3.7: Active impedance and active reflection coefficient of cylindrical array with (a),(b) slot curved along the E-plane and (c),(d) along the H-plane, for different radii of curvature.

It can be noted that, also for this ultra-wideband unit cell, the effect of the curvature on the matching properties is more evident for arrays curved in the E-plane with respect to arrays curved in the H-plane. As a consequence, a stronger curvature can be used in the H-plane with no strong deviation of the active matching properties from the planar case. Moreover, the variation of the active impedance with M is strongly frequency dependent. In fact, at the lowest frequency of investigation and for the cylindrical E-plane array, a large $M \geq 30$ is necessary to fully converge to the performance of the planar array (active $|\Gamma| \approx -10$ dB). The behavior at higher frequency is more similar to the planar array for smaller $M \approx 16$.

Thus, we can conclude that the deviation of the cylindrical array from the planar array is related to the radius of curvature array with respect to the wavelength and to the polarization of the slots along the cylinder curvature.

3.3 Radiation Pattern of Wideband Cylindrical Array

In this section, the method in Appendix A is implemented to construct the radiation pattern of the ultra-wideband cylindrical array from the unit cell simulation. First, Fig. 3.8 shows the pattern of the E-plane curved slot unit cell, with $M = 8$, dimensions as in Table 2.2, and dielectric slabs defined in Table 3.1. The pattern is presented in the elevation plane $\phi = 0°$ and in the azimuth plane $\theta = 90°$. In addition, the pattern of its adjacent element is obtained in post-processing by

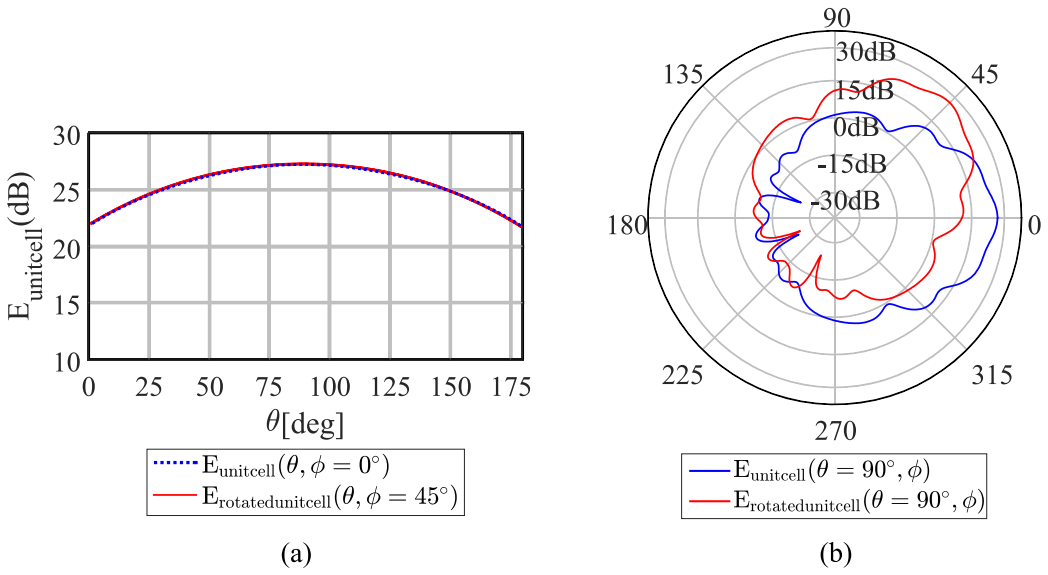

Figure 3.8: Radiation patterns cuts of ultra-wideband unit cells before and after rotation by α in the (a) elevation and (b) azimuth planes.

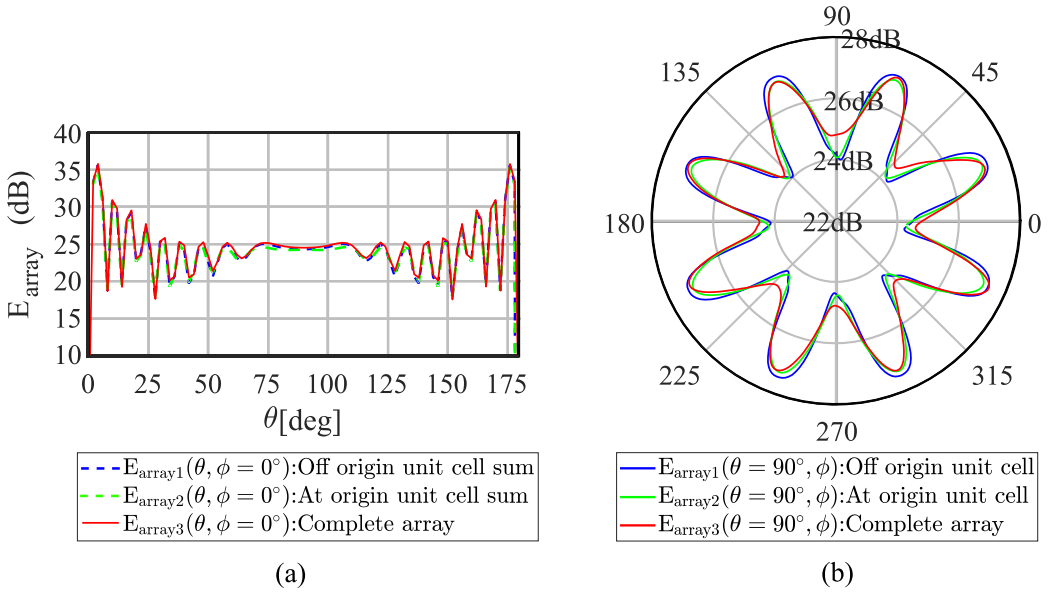

Figure 3.9: Radiation patterns cuts of ultra-wideband cylindrical array calculated from unit cell and complete ring simulations in the (a) elevation plane and (b) azimuth plane.

applying azimuthal rotation by $\alpha = 45°$, as shown in Fig. 3.8(b).

The radius of the cylindrical array for the ultra-wideband unit cell is $R = r_a + h_{\text{br}} + \sum h_{\text{dielectric}}$. The pattern of the array can be found with the procedure described in Appendix A. Two choices of the reference systems, one with the origin at the element feed and another with the origin at the center of the cylinder, are considered. Fig. 3.9 shows the same results of both choices of the reference system as well as the complete array simulation in the elevation plane $\phi = 0°$ and in the azimuth plane $\theta = 90°$.

It can be observed that the pattern of the cylindrical array, with all elements excited in phase, is nearly omnidirectional. However, because of the thick dielectric superstrates, the arc length of each unit cell at the outer surface of the most external slab is larger than lambda. This causes some oscillations in the pattern of approximately 3 dB.

In practical applications, the patterns generated by the cylindrical arrays are not omnidirectional, but only a portion of the antenna array is actively used to generate a directive beam, with the proper phase excitation to focus the beam in a certain direction. The excitation required to generate directive beams is strongly non-periodic; thus, it cannot be assessed with periodic unit cell simulations. For this reason, in the following chapters, we study the performance of finite truncated cylindrical arrays, or entire cylindrical arrays where only a portion of the elements are actively excited, while the rest of the array is terminated on resistive loads.

4. Phase Excitation Method

The patterns of a periodic cylindrical array shown in the previous chapter are omnidirectional in the azimuth plane. This is because, in the periodic environment, all elements on a ring of the array are excited simultaneously with equal phases, thus achieving an omnidirectional radiation pattern.

To obtain a highly directive beam from the cylindrical array, one can excite only a finite portion of the array with proper phases to compensate for the curvature. This chapter introduces a method to find the input phases required for scanning finite cylindrical arrays. Phase excitations of the finite cylindrical array are studied for both wideband (without superstrates) and ultra-wideband (with superstrates) connected slots. In addition, ray tracing is also applied in the anisotropic dielectric slabs of the wideband cylindrical array, as in [37, 38]. Despite including the effects of the inhomogeneous slabs on the phase distribution, the ray tracing method does not take into account the mutual coupling, the edge effects, and the impedance variation across the array. Therefore, a more suitable estimation of the phases can be performed with a full-wave simulation of the entire array under plane-wave incidence.

4.1 Element Phases in Finite Cylindrical Array

The typically array phase distribution required for scanning in cylindrical arrays can be defined by geometrical considerations. For a planar array, as shown in Fig. 4.1(a) and (b), the elements can transmit or receive simultaneously with no time delay (i.e., no phase shift in the frequency domain) to generate a planar wavefront for broadside scanning. Unlike the planar array, the elements of a cylindrical array require phase shifts to match a planar wavefront, as schematically shown in Fig. 4.1(c) and (d). The phase shifts follow a quadratic distribution to compensate for the different positions of the elements along a circle. The phases required for an array in transmission (TX) are the conjugates of the phases of the array in reception (RX).

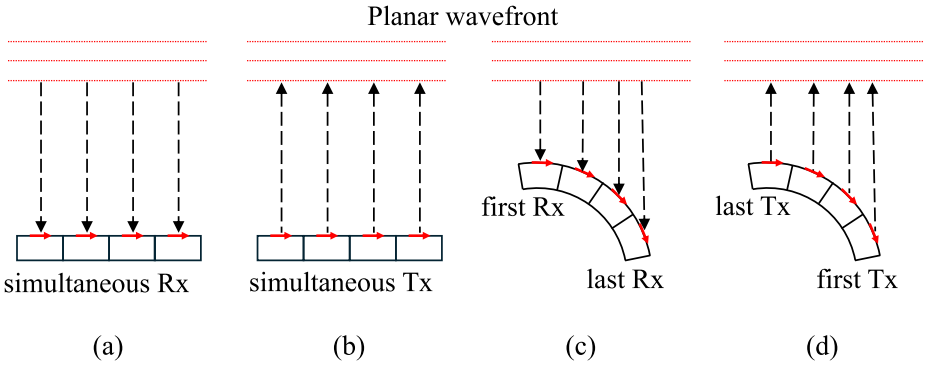

Figure 4.1: Reception and transmission of a plane wave on a planar array (a),(b) and a cylindrical array (c),(d) are schematically shown.

As an example, a finite cylindrical array with 8 connected slots is simulated in HFSS, with the feed points represented by the red arrows in Fig. 4.2(a). The unit cell curvature is defined by $\alpha = \pi/16$, while all other dimensions are defined as in Table 2.2. The ports are numbered from 1 to 8, as shown in the figure. Then, the phase at each port needs to be defined for the broadside radiation ($+z$ direction).

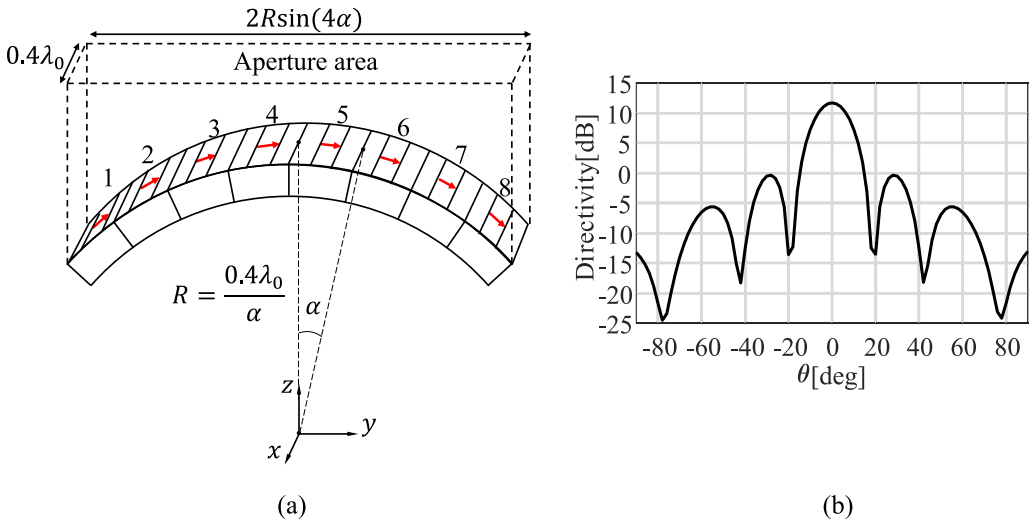

(a) (b)

Figure 4.2: (a) Finite cylindrical array with 8 elements along the cylinder curvature and (b) E-plane directivity pattern at frequency f_0.

The phases of the array elements can be found by considering the expression of the propagation vector for a certain direction θ_0, ϕ_0

$$\vec{k} = k\sin\theta_0\cos\phi_0\hat{x} + k\sin\theta_0\sin\phi_0\hat{y} + k\cos\theta_0\hat{z} \tag{4.1}$$

where $k = 2\pi/\lambda_0$ is the propagation constant of free space and λ_0 is the wavelength at the calculation frequency f_0. The position of the array element with index m can be expressed as

$$\vec{r}_m = R\sin\left(\frac{2m-M-1}{2}\alpha\right)\hat{y} + R\cos\left(\frac{2m-M-1}{2}\alpha\right)\hat{z} \tag{4.2}$$

where $m \in 1, 2, ...8$ and the radius $R = 0.4\lambda_0/\alpha$ is the distance from the feeding point to the cylinder axis. The phases of the elements to scan in a certain direction θ_0, ϕ_0 are given by

$$\beta_m(\theta_0, \phi_0) = -\vec{k}\cdot\vec{r}_m \tag{4.3}$$

which, for broadside scanning, becomes

$$\beta_m(\theta_0 = 0°, \phi_0) = -kR\cos\left(\frac{2m-M-1}{2}\alpha\right). \tag{4.4}$$

For example, the element phases for broadside radiation at the calculation frequency f_0 for this finite cylindrical array are shown in Table 4.1. These phases are given as input excitations in the finite array simulation in HFSS, resulting in the E-plane directivity pattern in Fig. 4.2(b). The maximum broadside directivity is about 11.7 dB, which is close to the maximum directivity from the projected aperture area of the array. As seen in Fig. 4.2(a), the aperture of the finite cylindrical array is the projected planar area A that is orthogonal to the broadside direction. Then the maximum directivity $D_{\max}$ can be calculated as follows [36]:

$$A = 2R\sin(4\alpha) \times 0.4\lambda_0 \tag{4.5}$$

$$D_{\max} = \frac{4\pi A}{\lambda_0^2} \approx 11.6\text{dB} \tag{4.6}$$

The maximum directivity calculated by the formula is nearly equal to the simulated array directivity; thus, for the free-space array, the given method is sufficient to estimate the needed element phases to achieve maximum broadside directivity. However, such a procedure is not effective for the wideband finite cylindrical array, which requires more complex approaches.

Table 4.1: Phase of broadside radiation of finite cylindrical array

Element index	1	2	3	4	5	6	7	8
Phase [deg.]	0	-80	-135	-163	-163	-135	-80	0

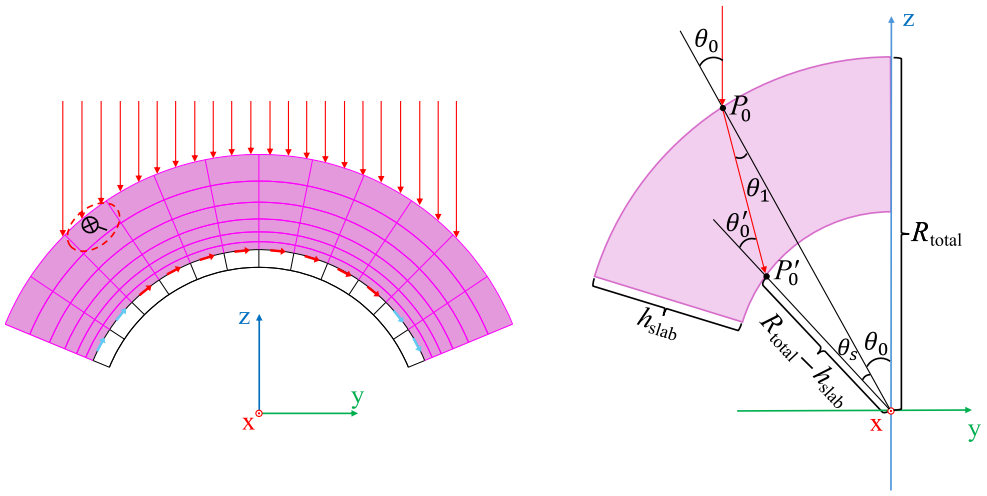

Figure 4.3: (a) Wideband finite cylindrical array with 8 active elements and 4 dummy elements and (b) Snell's law applied at the slab interfaces.

4.2 Element Phases in Wideband Finite Cylindrical Array

To study a wideband array, we now consider the same structure introduced in Chapter 3, where homogeneous anisotropic dielectric slabs equivalent to ADLs are located above the slots. The array is truncated to 12 elements, with 8 active ports and 4 dummy ports, 2 on each side, as shown in Fig. 4.3(a). The dummy ports are included to reduce edge effects and improve the matching performance of the edge elements.

4.2.1 Ray Tracing Method

Unlike the free space array, the presence of the dielectric slabs and the dummy element makes it more difficult to define the aperture area of the array. The slabs increase the overall volume occupation of the array. Moreover, because of the inhomogeneity of the entire superstrate made of different slabs, the ray picture adopted in Fig. 4.1(d) cannot be used for the wideband array. The ray tracing method is applied assuming an incident plane-wave traveling in the $-z$-direction, as seen in Fig. 4.3(a). For each ray of the incident plane wave, Snell's law is applied at each slab interface to derive the angles of the ray in each cylindrical slab. The geometry of the problem is defined in Fig. 4.3(b).

The initial incident angle is θ_0, ranging from -4α to 4α. The initial incident position $P_0 = (0, R_{\text{total}} \sin\theta_0, R_{\text{total}} \cos\theta_0)$. To find the transmitted ray inside the dielectric slab, the angle of refraction θ_1 is found by the Snell's law:

$$n_0 \sin\theta_0 = n_1 \sin\theta_1 \,. \tag{4.7}$$

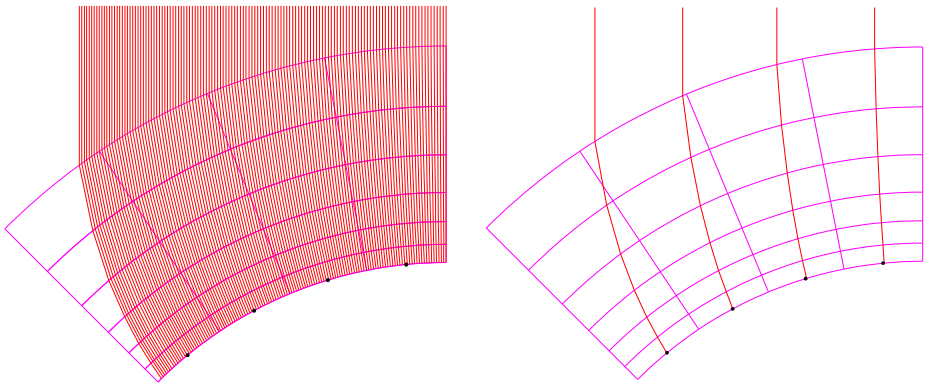

(a) (b)

Figure 4.4: (a) Ray tracing in the array superstrate, with dense sampling and (b) rays that eventually end at the array feed points.

Table 4.2: Phase of broadside radiation of finite cylindrical array

Element index	1	2	3	4	5	6	7	8
Phase [deg.]	0	-83	-142	-171	-171	-142	-83	0

Using (3.1), we can relate the angles to the tensor permittivity and permeability of the slabs as

$$n_0 = 1,\ n_1 = n_{\mathrm{TM}} = \sqrt{\varepsilon_x \mu_y + (1 - \varepsilon_x/\varepsilon_z)\sin^2\theta_0} \tag{4.8}$$

$$\theta_1 = \mathrm{asin}\left(\frac{n_0 \sin\theta_0}{n_{\mathrm{TM}}}\right). \tag{4.9}$$

Then the incident angle at the next dielectric slab interface θ_0' can be found by the law of sines:

$$\frac{\sin(\pi - \theta_0')}{R_{\mathrm{total}}} = \frac{\sin\theta_1}{R_{\mathrm{total}} - h_{\mathrm{slab}}}. \tag{4.10}$$

Using the identity $\sin(\pi - \theta_0') = \sin\theta_0'$ and knowing that the angle $\theta_s = \theta_0' - \theta_1$, the end point of the ray inside the slab can be found as $P_0' = (\,0, (\mathrm{R_{total}} - \mathrm{h_{slab}})\sin(\theta_0 + \theta_s), (\mathrm{R_{total}} - \mathrm{h_{slab}})\cos(\theta_0 + \theta_s)\,)$. This procedure can be applied recursively at all other slab interfaces to obtain the ray in the entire anisotropic superstrate. The resulting rays are plotted in Fig. 4.4. First, a large number of rays is calculated in the structure, as depicted in Fig. 4.4(a), and subsequently only the rays that end at the feeding points of the array are extracted, as shown in Fig. 4.4(b).

The rays intersecting the feed points can be used to calculate the optical paths inside the dielectric slabs, and the corresponding phases associated with the elements. These phases are calculated by multiplying the free-space wavenumber k by the total optical path length (OPL) of the ray. The total OPL is the sum of the terms $(n_i\overline{P_0P_0'})$ for the different segments $\overline{P_0P_0'}$ of the ray in each slab with effective refractive index n_i. The computed phase for each element is shown in Table 4.2.

When comparing these phases with the ones in Table 4.1, it is apparent that the phases calculated with the ray tracing do not deviate a lot from the free-space case. Although the path in dielectric slabs for the edge elements seems much longer than the path for the center elements, the refractive index is smaller for oblique rays (large θ_0) compared to normal rays ($\theta_0 = 0°$), and thus the total optical path for each ray remains similar.

The phases calculated from an ideal free-space array and from the ray tracing approach are applied to the elements of the array in HFSS to compute the radiation pattern. The resulting

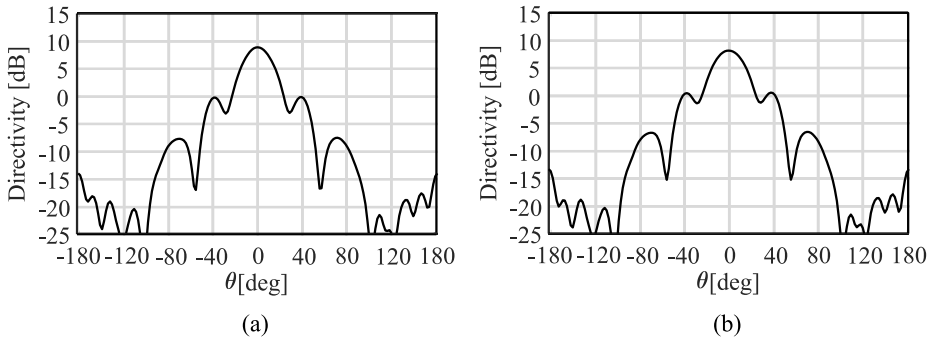

Figure 4.5: Directivity pattern of the cylindrical array when element phases are computed (a) with the array factor in free space and (b) with the ray-tracing approach.

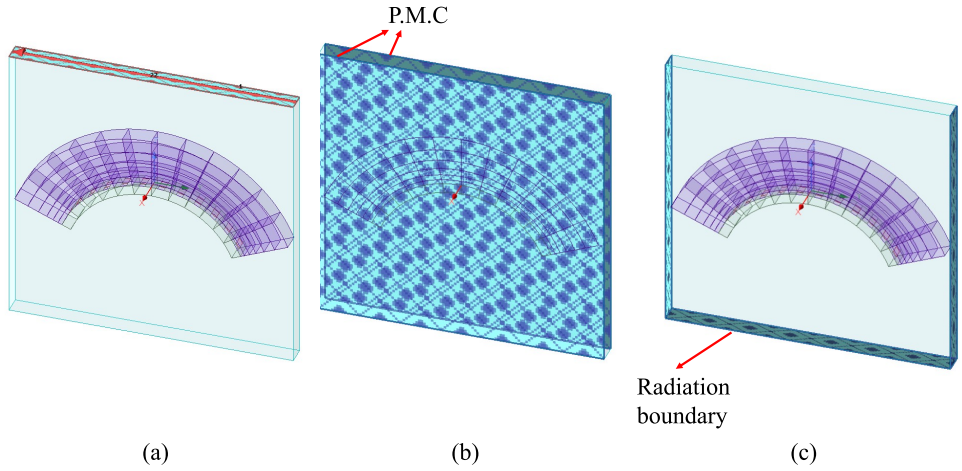

Figure 4.6: Receiving array simulated in HFSS: (a) Lumped port above to simulate an incident plane wave, (b) P.M.C boundaries to synthesize the equivalent periodicity, and (c) radiation boundary.

directivity patterns are shown in Fig. 4.5(a) and (b). It can be observed that the patterns are very similar and the directivity is lower than 10 dB, which is significantly lower than the maximum theoretical directivity from the array aperture. For this reason, a more accurate method is introduced to account for the mutual coupling between elements and the edge effects.

4.2.2 Array Simulation in Reception

The method proposed here consists of simulating the entire finite array in HFSS under plane-wave incidence, with the ports of the elements terminated on resistive loads. The complex values of the received electric field are probed at the ports to find the phases of the received voltages in the feeding gaps. The complex conjugates of these phases are subsequently used in the simulation of the array in transmission to generate the planar wavefront in the same direction.

The simulation of the array in reception is set in HFSS, as described in Fig. 4.6. A lumped port is defined over the entire aperture above the array, to obtain a plane-wave-like incident field [Fig. 4.6(a)]. The array feeds are replaced with 50Ω resistors that represent the receiving loads. The side walls orthogonal to the cylinder axis are assumed to be made of a perfect magnetic conductor (P.M.C) to synthesize periodic excitation [Fig. 4.6(b)]. This is equivalent to having periodic boundary conditions for normal incidence, with the advantage that the P.M.C boundaries allow the

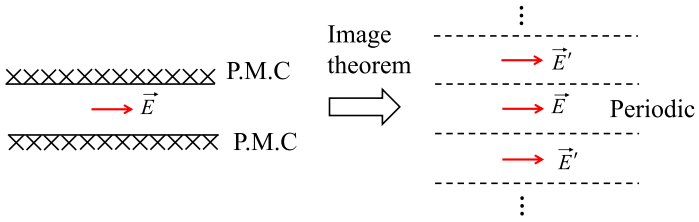

Figure 4.7: Image theorem to obtain the equivalent periodic electric fields.

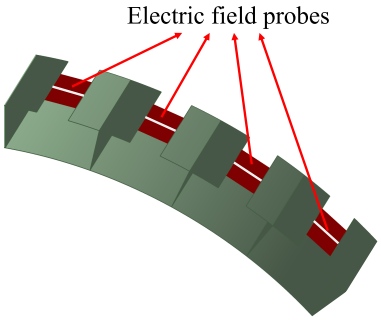

Figure 4.8: Electric field probes for phase calculation.

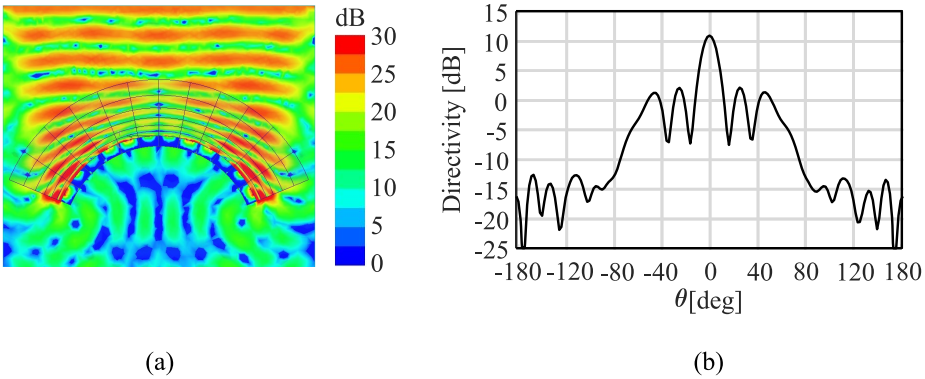

Figure 4.9: (a) Electrical field distribution for the array simulation in reception and (b) directivity pattern of the array in transmission.

lumped port to touch the boundary. The other two side walls and the bottom wall of the volume are assigned radiation boundary conditions [Fig. 4.6(c)]. The equivalence between the P.M.C and the Floquet boundary conditions is illustrated in Fig. 4.7. This shows the top view of the problem with the uniform electric field impressed between the P.M.C walls and oriented parallel to the walls. By applying the image theorem, the walls can be replaced by an infinite set of images of the same electric field to form a uniform and infinitely extended field distribution.

Moreover, electric field probes can be defined as lines in the center of the 50Ω surface resistances at the receiving gaps in the slots, as shown in Fig. 4.8. The complex electric field values can be computed on these lines, providing the phase of the component of the field projected parallel to the lines: $\beta_m = \angle(\vec{E}(\vec{r}_m) \cdot \hat{t}_m)$, where $\vec{E}$ is the complex electric field vector at the m-th feed location and $\hat{t}_m$ is the tangential unit vector aligned with the corresponding probing line. The conjugate phase distribution is then used in transmission to obtain a directive pattern in the same direction as the incident plane-wave in the receiving case.

Table 4.3: Phase of broadside radiation of finite cylindrical array

Element index	1	2	3	4	5	6	7	8
Phase [deg.]	0	48	-84	-63	-63	-84	48	0

The electric field distribution obtained from the array simulation in reception is shown in Fig. 4.9(a). It can be observed that the electric field is strong at the edge dummy elements; thus, it is important to include the edge effect for accurate estimation of the element phases for both reception and transmission. The conjugate phases obtained from the simulation are shown in Table 4.3, at the frequency f_0. Unlike the phases calculated with the previous method, the phase values do not seem to follow the typical quadratic distribution. This is a consequence of the mutual coupling and the edge effects. Using these phases, the directivity pattern in Fig. 4.9(b) is obtained. The pattern has a narrower beamwidth compared to the results in Fig. 4.5, and the maximum directivity is now increased to about 11 dB, despite a higher sidelobe level.

Since the mutual coupling affects the radiation pattern and the active input impedance of the array elements, the phases calculated with the proposed method will be used in the following chapter to study the performance of the finite cylindrical array.

This Page Intentionally Left Blank

5. Performance of Finite Cylindrical Arrays

The previous chapter discussed methods aimed at finding the excitation phases of finite cylindrical arrays to form a directive beam. To achieve higher directivity, a simulation of a finite-by-infinite array was performed under plane wave illumination. The phases of the incident electric field in the gaps can then be used after complex conjugation for the array in transmission. This procedure is convenient because it accounts for the mutual coupling between ports and the finite edge effects. In this chapter, the procedure is used to study the performance of the finite cylindrical array.

5.1 Edge Effects of Finite Cylindrical Array

Antenna efficiency is defined as the ratio between the radiated and the input power. For connected arrays of slots that target ultra-wide bandwidth and wide scan range, the main cause of inefficiency is the impedance mismatch loss. Therefore, the efficiency analysis reported here focuses mainly on matching efficiency. In wideband arrays, the broadband behavior is achieved by means of high inter-element coupling. However, the high mutual coupling also causes large frequency variations of the active input impedance of the array elements. To assess the collective performance of the finite array, we use the matching efficiency, calculated as follows:

$$\eta_{\text{matching}} = \frac{P_{\text{in}} - P_{\text{refl}}}{P_{\text{in}}} \tag{5.1}$$

where P_{in} is the total input power for all elements of the array and P_{refl} indicates the total power reflected at all ports. The power can be related to the amplitudes of the incident (V_m^+) and reflected (V_m^-) voltage waves at the antenna ports as follows:

$$P_{\text{in}} = \sum_{m=1}^{M} \frac{1}{2} \frac{|V_m^+|^2}{Z_0} \tag{5.2}$$

$$P_{\text{refl}} = \sum_{m=1}^{M} \frac{1}{2} \frac{|V_m^-|^2}{Z_0} = \sum_{m=1}^{M} \frac{1}{2} \frac{|V_m^+ S_{m,\text{active}}|^2}{Z_0} \tag{5.3}$$

where Z_0 is the port normalization impedance of the array elements and $S_{m,\text{active}}$ is the active reflection coefficient at the m-th terminals, computed as:

$$S_{m,\text{active}} = \sum_{i=1}^{M} S_{mi} \frac{V_i^+}{V_m^+} \tag{5.4}$$

If the input power is equal at each feed and set as 1 W for all M active ports, we can express the efficiency as

$$\eta_{\text{matching}} = 1 - \frac{1}{M} \sum_{m=1}^{M} |S_{m,\text{active}}|^2 \,. \tag{5.5}$$

To assess the edge effects of the finite array, we consider HFSS simulations of a finite-by-infinite array, finite in the E-plane and periodic in the H-plane. For the sake of comparison, both the planar array and the curved cylindrical array structures are simulated, as shown in Fig. 5.1(a) and (b). Both arrays are assumed to include 8 active elements and 4 dummy elements (2 at each edge). The size of the array is electrically small at the lowest frequency of analysis, resulting in poor efficiency [39]. In the study of the matching efficiency, the phases of the cylindrical array are selected based on the method described in Sec. 4.2.2.

The PML boundary of the finite planar array is set with four parallelepipeds that form a rectangular frame [see Fig. 5.1(a)], while the PML boundary of the finite cylindrical array is set for each unit cell over a cylindrical surface. It is not necessary to further split the PML before because $\alpha = \frac{2\pi}{32}$ is a fairly small angle, thus each PML boundary can be approximated as locally flat.

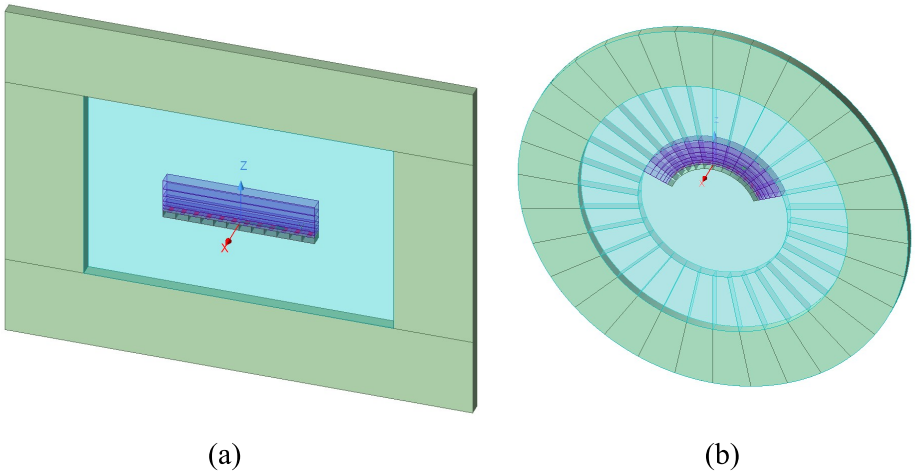

Figure 5.1: Finite-by-infinite simulations of (a) planar and (b) cylindrical array in HFSS.

Table 5.1: Phase of broadside radiation of finite cylindrical array

	$0.1f_0$	$0.4f_0$	$0.7f_0$	f_0
port 1	0°	0°	0°	0°
port 2	−3°	−13°	−51°	48°
port 3	−5°	−39°	−47°	−84°
port 4	−6°	−56°	−94°	−63°

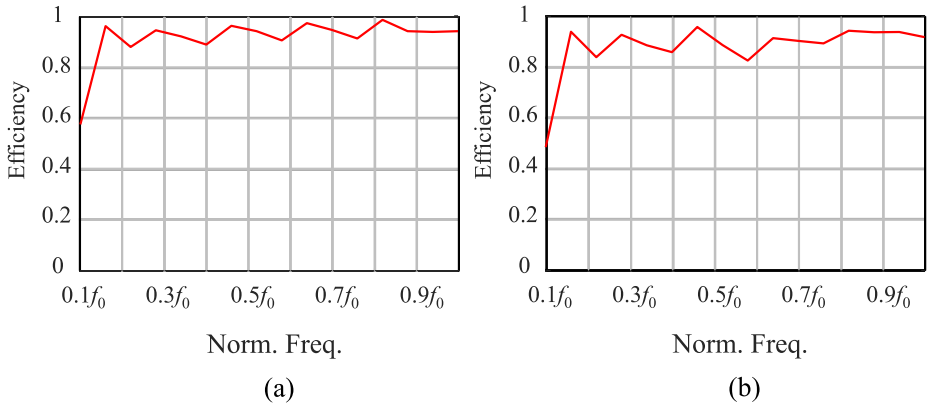

Figure 5.2: Matching efficiency of the finite (a) planar and (b) cylindrical array, for broadside radiation.

5.1.1 Matching Efficiency

The matching performance of both finite arrays is simulated for broadside scanning. It is important to note that the element phases required for broadside radiation are frequency dependent for the finite cylindrical array. Thus, for every frequency, different input phases are considered for the feeds as shown, for example, in Table 5.1 for the frequencies $0.1f_0$, $0.4f_0$, $0.7f_0$, f_0. For the planar array case, all phases are simply set to zero independently of the frequency.

As seen in Fig. 5.2(a) and (b), the matching efficiency for broadside radiation shows comparable results for both the planar and cylindrical finite arrays. The matching efficiency is over 80% in most of the frequency band, except for the lowest frequency, for which the entire array becomes half a

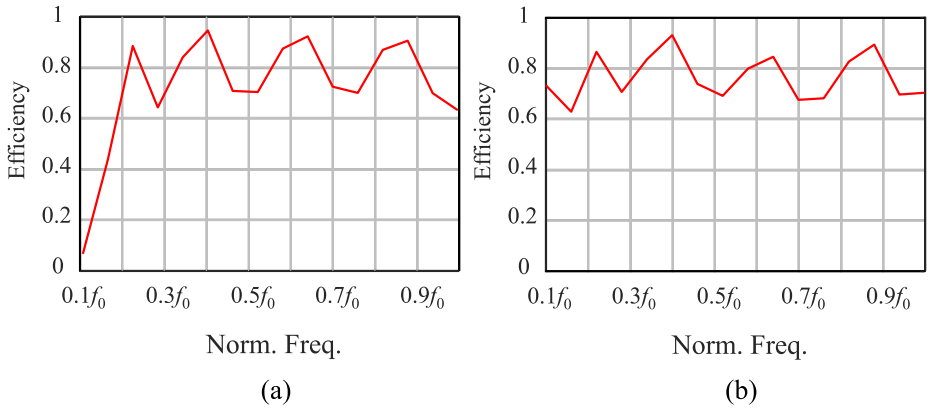

Figure 5.3: Matching efficiency of the finite (a) planar and (b) cylindrical array, for 60 degrees scanning in the H-plane.

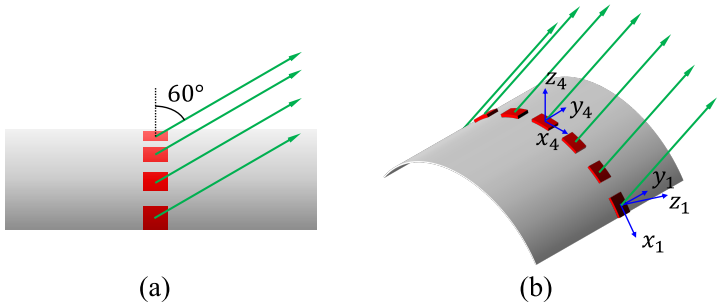

Figure 5.4: (a) Side view and (b) 3D view of the elements with local reference system and scanning to 60 degrees in the H-plane.

wavelength in length.

The performance of the arrays when scanning to 60 degrees in the H-plane is presented in Fig. 5.3(a) and (b). As expected, the scanning matching efficiency for both arrays is worse than in the broadside case. The efficiency is higher than 60% for the planar array, except at low frequencies, where it drops to 10%. However, for the finite cylindrical array, the matching efficiency remains above 60% even at the lowest frequency. One possible explanation for this effect is that the elements on the cylindrical surface do not scan in the same direction with respect to the local normal. This aspect is described in Fig. 5.4, where it can be observed that, while an element in the center of the array would scan to $\phi_4 = 90°, \theta_4 = 60°$ according to the local reference system (x_4, y_4, z_4), an element at the edge of the array would scan to $\phi_1 \approx 70°, \theta_1 \approx 67°$ according to the local reference system (x_1, y_1, z_1). As a consequence, the matching condition can change according to the local periodicity.

5.1.2 Radiation Patterns for H-plane Scanning

Although the matching efficiency of the cylindrical array appears to be better than that of the planar array for scanning, the total efficiency must also be compared. The total efficiency is the product of the matching and the radiation efficiency. Radiation efficiency can be lower than 1 because of the dummy elements that can dissipate power in their resistive loads. In this regard, the difference between directivity and gain of the two arrays is shown in Fig. 5.5. Radiation patterns are provided in terms of directivity, gain, and realized gain for both arrays at the lowest frequency of 0.1 f_0.

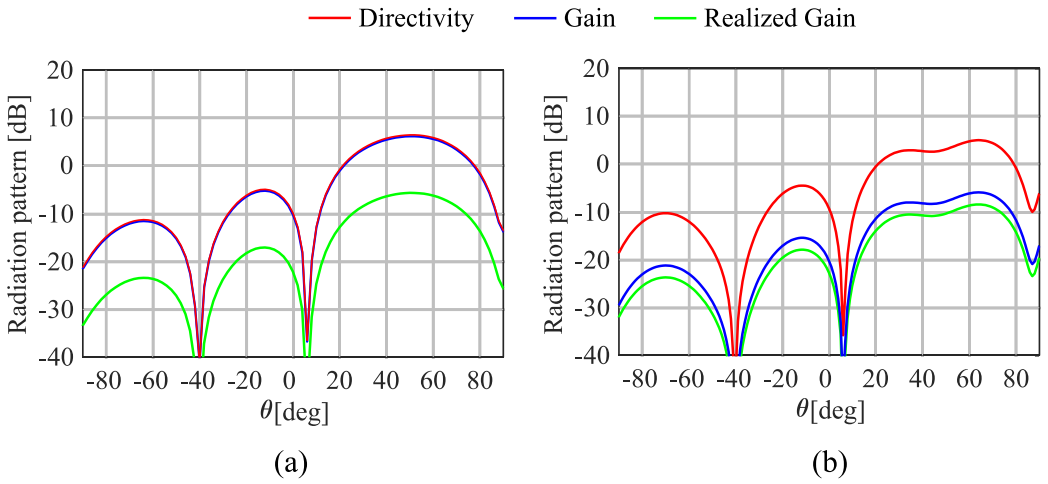

Figure 5.5: Directivity, gain and realized gain pattern of (a) finite planar array and (b) cylindrical array at $0.1f_0$.

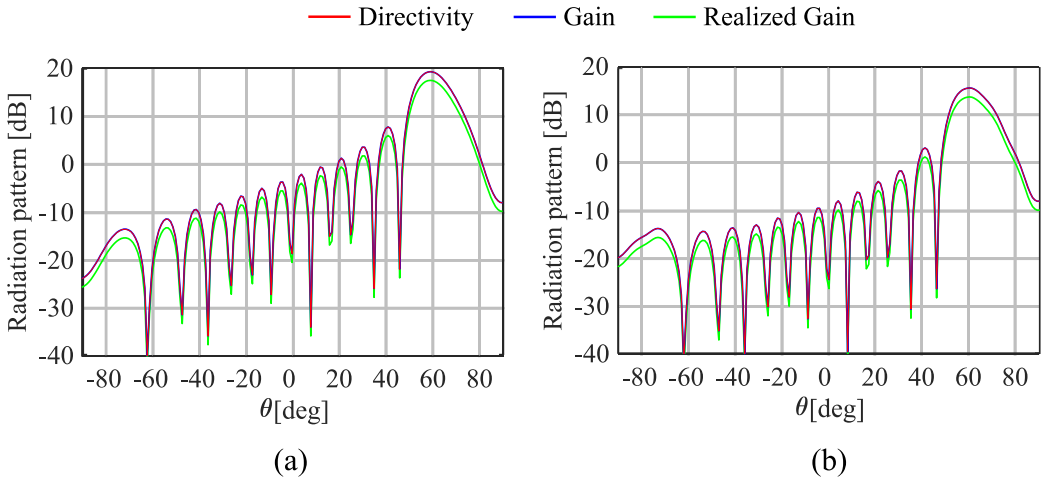

Figure 5.6: Directivity, gain and realized gain pattern of (a) finite planar array and (b) cylindrical array at $0.5f_0$.

An array factor with 32 elements is assumed in the H-plane, and the patterns are evaluated with the windowing approximation [40]. Both finite planar array and cylindrical array have realized gain about 12 dB lower than their directivity, which corresponds to an efficiency below 10%. For the planar array in Fig. 5.5(a), the directivity has the same value as the gain, while the realized gain is low, which indicates that all the losses are due to impedance mismatch. In contrast, for the cylindrical array, both the gain and the realized gain are low, which corresponds to 70% matching efficiency and about 14% radiation efficiency. We can conclude that, while the cylindrical array shows better matching performance than the planar array when scanning, the total efficiency is not improved due to large dissipation losses in the resistors of the dummy elements.

The patterns for scanning to 60 degrees in the H-plane at the middle frequency ($0.5f_0$) and the highest frequency (f_0) are shown in Fig. 5.6 and Fig. 5.7, respectively. At these frequencies, the directivity equals the gain for both planar and cylindrical arrays; thus, there is no power dissipation in the dummy elements. The realized gain is 1.5 dB lower than the directivity, in line with the

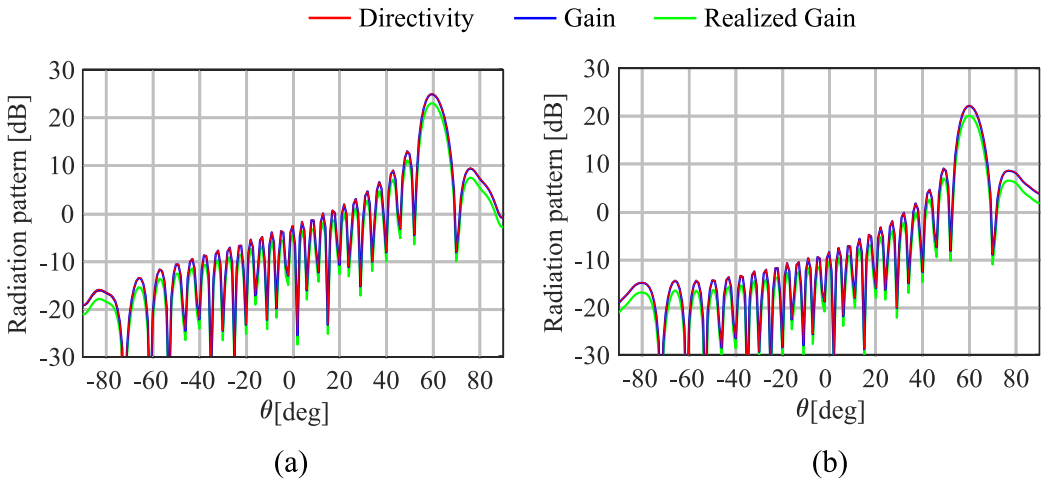

Figure 5.7: Directivity, gain and realized gain pattern of (a) finite planar array and (b) cylindrical array at f_0.

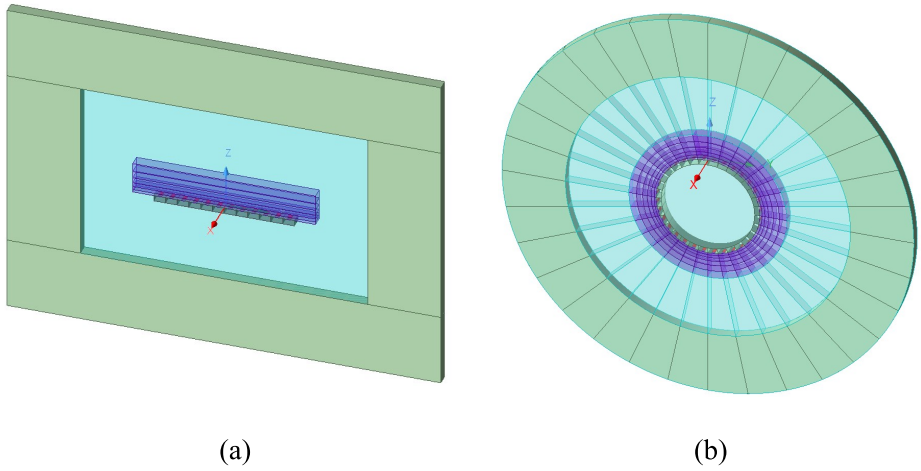

Figure 5.8: A finite planar array with extended dielectric slabs (a) and a complete ring finite array with 32×32 elements (b) are modeled in HFSS.

matching efficiency of 70%.

In addition, the realized gain of the finite cylindrical array is always lower than that of the finite planar array for every frequency because, for the same number of elements, the effective aperture of the cylindrical array is always smaller after projection.

5.2 Study of Complete Ring Finite Array

To study the performance of the arrays for scanning in the E-plane, two different structures are considered. For the planar array, we assume that the dielectric substrates extend outside the radiating aperture, as can be seen in Fig. 5.8(a). To fully highlight the advantage of cylindrical arrays with respect to planar ones, we consider the cylindrical array without truncation, forming an entire ring, as shown in Fig. 5.8(b). The extension of the superstrate in the planar array is made such that the two geometries have the same total projected length along y. The purpose of the extended

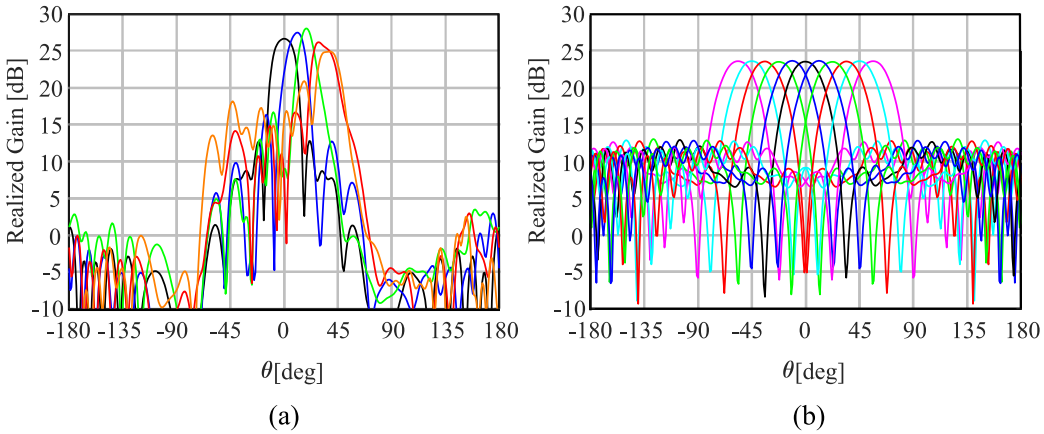

Figure 5.9: Directivity pattern of 8 active elements on the finite planar array (a) and 8 active elements on the complete ring finite array (b) are simulated for E-plane scanning at f_0.

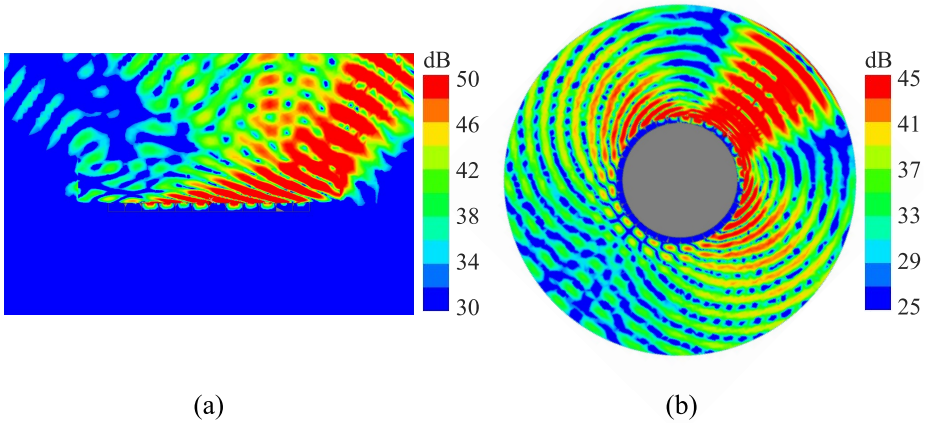

Figure 5.10: Electric field map for scanning to 40 degrees in E-plane of (a) the finite planar array and (b) the cylindrical array in HFSS.

dielectric slabs is to mitigate strong reflections that occur at the edges of the thick dielectric when scanning to large angles in the E-plane.

In the complete circular array, there are 32 elements along the cylinder curvature, which give $\alpha = \frac{2\pi}{32}$. Note that, for a certain beam, only 8 elements are excited in the complete ring, while the other 24 elements are dummy elements. The scanning in the E-plane is then realized by exciting 8 elements in different parts of the array.

5.2.1 Radiation Patterns for E-plane Scanning

The comparison of realized gain patterns of both arrays scanning in the E-plane is shown in Fig. 5.9. The scanning of a planar array is achieved by progressive phase delay, while the scanning of the ring array is achieved by exciting the elements on the different parts of the array, with the same phases. The result of the planar array scanning up to 40 degrees in the E-plane is presented in Fig. 5.9a. It can be seen that the realized gain for scanning to 20° is larger than the one at broadside. This could be explained with the fact that the dielectric superstrates can support leaky waves that enhance the gain in some directions in the far field. For larger scan angles, the patterns degrade, both in terms

of maximum gain and sidelobe level.

On the other hand, the complete ring array does not have scan loss and it is capable of scanning with constant realized gain over the entire azimu th [Fig. 5.9(b)]. The patterns are characterized by evenly distributed sidelobes over the entire azimuth range. To visualize this effect, the near-field electric field distribution of the arrays is presented in Fig. 5.10. For the planar array field distribution, the diffraction from the edges can be appreciated, which contributes to the pattern degradation and the increased sidelobe level. Also, from the field distribution of the cylindrical array, the evenly distributed radiation in directions away from the main beam can be noticed.

This Page Intentionally Left Blank

6. Conclusions and Future Work

6.1 Summary and Conclusions

This thesis presented a study of conformal (cylindrical) connected slot arrays. The slots were considered to be radiating in the presence of a backing reflector, either in free space or loaded with multiple anisotropic dielectric superstrates to achieve ultra-wideband matching properties. Different aspects were investigated and led to several relevant insights that can be summarized as follows.

- **Unit Cell Simulations in HFSS and Implementation of PML**
  A procedure was derived to simulate a periodic unit cell of a cylindrical array with Ansys HFSS. The periodic Floquet boundaries can be tilted to form an angle α that is related to the radius of curvature. One of the main challenges that occurred was the definition of the perfectly matched layer (PML), necessary to approximate the radiation boundary condition. The default PML boundary available in HFSS, although working well for planar unit cells, does not function properly for curved unit cells. This issue was attributed to the definition of the PML's axes of anisotropy, which are fixed and do not follow the curved boundary. Two solutions were proposed to this problem. The first consisted of defining multiple PMLs for smaller sectors of the unit cell, thus better following the curvature. The second involved the inclusion of an isotropic absorber with electric and magnetic properties defined to avoid reflections.

- **Active Input Impedance vs Radius of Curvature**
  The active input impedance of connected array unit cells was studied for varying radii of curvature. As expected, the active impedance of a cylindrical array converges to that of the corresponding planar array for a large radius of curvature. However, the convergence rate is different for arrays curved in the E-plane or in the H-plane. More specifically, arrays curved in their E-plane require larger radii of curvature to be approximated as locally flat and to converge to the planar array performance. Moreover, when considering very large frequency bands ($\sim$10:1), the cylindrical array behavior deviates more from the planar counterpart at the lower frequencies of operation, for which the radius of curvature is smaller compared to the wavelength.

- **Phase Excitation of the Cylindrical Array**
  The radiation pattern of a periodically excited cylindrical array has low directivity since it is omnidirectional in the azimuth plane. To realize directive beams, a finite curved array was simulated and excited with non-periodic weights. A quadratic phase distribution is needed to compensate for the curvature and achieve a planar radiated wavefront. For connected arrays in free space, the ideal phases can be calculated from simple geometrical considerations. However, when the thick superstate is added to the array to achieve wide bandwidth, the ideal phases do not provide high directivity. A ray tracing method was implemented to correct for the curved trajectories of the rays into the inhomogeneous superstrate. However, this correction has only minor effects on the phases and does not improve significantly the directivity. A more accurate method to estimate the phases was then proposed, based on a simulation of the complete array in reception under plane-wave incidence, to find the phases at the receiving feed of each element. The conjugate phases can then be used for the array in transmission. This method accounts for mutual coupling and edge effects and provides enhanced directivity.

- **Truncation Effects in Finite Cylindrical Arrays**
  The edge effects of finite curved arrays were studied, based on finite-by-infinite cylindrical array simulations. The performance was compared with finite planar arrays of comparable sizes, in terms of matching efficiency, directivity, and gain, for broadside and for scanning in the infinite plane. Although there seems to be an advantage with regard to matching for scanning to 60 degrees of cylindrical arrays at the lowest frequency, the total efficiency was found to be similar

to the planar array because a significant amount of power is absorbed in the dummy elements. Besides, the realized gain is lower than that of the planar array with the same number of elements, due to the smaller radiation aperture of the curved array. Alternatively, a complete ring array with 32 elements is analyzed for scanning to arbitrary angles in the E-plane by exciting 8 ports at the time for each beam direction. Such a configuration is shown to achieve constant gain for azimuth scanning, while the planar array can only scan up to about 40 degrees in the E-plane.

6.2 Future Work

This thesis constitutes the foundation for ongoing and future research activities:

- This work focuses on methods for simulating cylindrical array unit cells using commercial electromagnetic solvers. A possible future effort is the development of analytical models based on spectral domain methods with improved computational efficiency. Such methods would be convenient for extensive parametric analyses of cylindrical connected arrays, including both dipoles and slots, curved along the longitudinal or transverse plane.

- The wideband array unit cell studied in this work was simplified to allow for a faster simulation time. Because of this, the matching efficiency of the unit cell was not well optimized for large scanning angles. A possible future development is the study of a more realistic unit cell with optimized impedance matching performance. Such a unit cell would include the realistic feeding structure with a series capacitance and the real artificial dielectric layers made of patches.

- In practical applications, the cylindrical arrays would not be excited in a periodic way; thus, a numerical simulation of the entire finite array is needed to accurately assess the performance. In this regard, semi-analytical methods can be developed to simulate finite cylindrical arrays with reduced computational resources.

- The analysis shown in this work considered single-polarized slot elements, curved along their longitudinal (H) or transverse (E) plane. Dual-polarized cylindrical unit cells that combine the two configurations could also be analyzed to address the possible mutual coupling effects between orthogonal slots.

- Finally, the practical realization of cylindrical arrays is not trivial, due to the complexity of realizing non-planar printed circuit boards. The review and comparisons of convenient manufacturing technologies, based, for example, on 3D printing or additive manufacturing, can be the objective of future studies. The cylindrical array could also be approximated as a polygonal prism to enable multifaceted implementation of the curvature.

A. Appendix: Cylindrical Array Patterns

This appendix describes the procedure used to evaluate the radiation patterns of cylindrical arrays with HFSS. Different boundary conditions can be implemented in the HFSS unit cell simulations. These boundaries were compared in Fig. 2.6, in terms of active impedance, and can be summarized as follows:

- A single PML, which is a default boundary available in HFSS.
- Radiation boundary, also available as default boundary in HFSS.
- Split PML, obtained by dividing the unit cell into smaller sub-cells, each with a PML.
- User-defined absorber.

Although the best results in terms of impedance fluctuation were obtained with the split PML and with the absorber, to calculate radiation patterns, additional considerations must be made. The user-defined absorber does not allow one to calculate the pattern, since the radiated energy is dissipated before reaching the edge of the simulation volume. On the other hand, the split PML is a lengthy approach because it requires the manual setting up of a large number of boundary conditions.

For these reasons, it was decided to use the radiation condition for the calculation of the patterns. This boundary is the fastest to set up and is independent of the curvature and number of elements. Although the radiation boundary gives small fluctuations in the impedance, the resulting effects on the far-field radiation patterns were observed to be negligible.

Two methods are used to estimate the cylindrical array patterns, giving equivalent results. The first is based on a unit cell simulation [see Fig. A.1(a)], which is then combined with an array factor in post-processing to estimate the pattern of the complete ring. Alternatively, the entire array ring can be simulated [see Fig. A.1(b)], so that the pattern is obtained without the need for post-processing calculations. However, such a simulation requires larger computational effort.

A.1 Rotation of the Unit Cell Radiation Pattern

For example, the geometry in Fig. A.1(a) is considered, with $M = 8$ and $\alpha = 2\pi/M = \pi/4$. The reference system is chosen so that the slot axis is along z and the broadside direction of the unit cell is along x. The simulated electric far field from the unit cell is indicated as $\vec{E}(\vec{r})$, where the

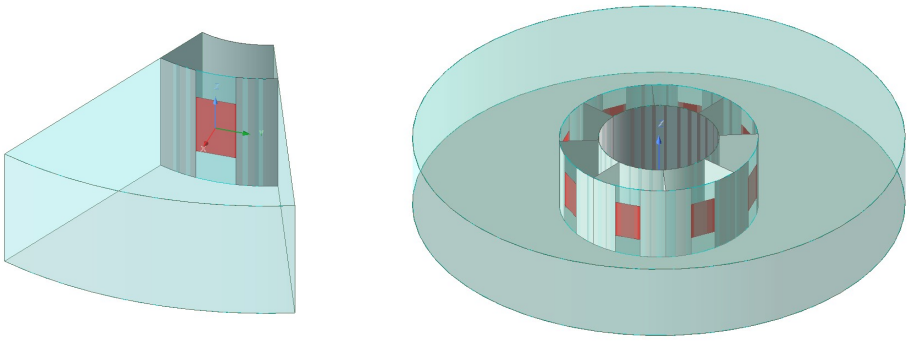

(a) (b)

Figure A.1: (a) Unit cell normal to the x-direction and (b) corresponding cylindrical array.

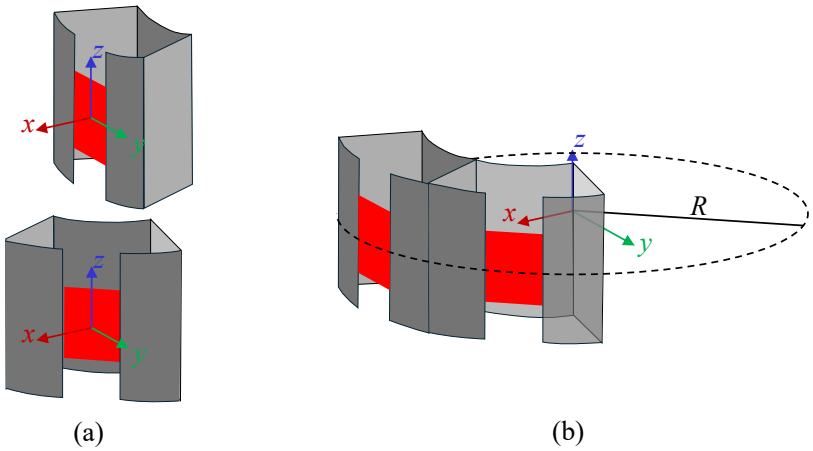

Figure A.2: (a) Unit cell set at the origin (b) Unit cell set off the origin

observation point is defined in the Spherical and Cartesian coordinate systems as

$$\vec{r} = \begin{bmatrix} r \\ \theta \\ \phi \end{bmatrix} \qquad \vec{r} = \begin{bmatrix} x \\ y \\ z \end{bmatrix} = \begin{bmatrix} r\sin\theta\cos\phi \\ r\sin\theta\sin\phi \\ r\cos\theta \end{bmatrix}. \tag{A.1}$$

Any other element of the array can be seen as a rotated version of this unit cell, as shown in Fig. A.2. Therefore, their pattern can be found by rotating $\vec{E}$ and $\vec{r}$. For this purpose, rotation matrices can be defined with respect to each of the Cartesian axes as follows:

$$\mathbf{R}_x(\gamma) = \begin{bmatrix} 1 & 0 & 0 \\ 0 & \cos\gamma & -\sin\gamma \\ 0 & \sin\gamma & \cos\gamma \end{bmatrix}, \ \mathbf{R}_y(\beta) = \begin{bmatrix} \cos\beta & 0 & \sin\beta \\ 0 & 1 & 0 \\ -\sin\beta & 0 & \cos\beta \end{bmatrix}, \ \mathbf{R}_z(\alpha) = \begin{bmatrix} \cos\alpha & -\sin\alpha & 0 \\ \sin\alpha & \cos\alpha & 0 \\ 0 & 0 & 1 \end{bmatrix} \tag{A.2}$$

where γ, β, and α represent the angles of rotation around the x-, y-, and z-axis, respectively. By applying the rotation on each of the axes, the observation vector $\vec{r}$ changes to $\vec{r}\,'$ as follows:

$$\vec{r}\,' = \mathbf{R}_z(\alpha)\vec{r} = \begin{bmatrix} r\sin\theta(\cos\phi\cos\alpha - \sin\phi\sin\alpha) \\ r\sin\theta(\cos\phi\sin\alpha + \sin\phi\sin\alpha) \\ r\cos\theta \end{bmatrix} = \begin{bmatrix} r\sin\theta\cos(\phi+\alpha) \\ r\sin\theta\sin(\phi+\alpha) \\ r\cos\theta \end{bmatrix} = \begin{bmatrix} r\sin\theta'\cos\phi' \\ r\sin\theta'\sin\phi' \\ r\cos\theta' \end{bmatrix} \tag{A.3}$$

$$\vec{r}\,' = \mathbf{R}_y(\beta)\vec{r} = \begin{bmatrix} r\sin\theta\cos\phi\cos\beta + r\cos\theta\sin\beta \\ r\sin\theta\sin\phi \\ -r\sin\theta\cos\phi\sin\beta + r\cos\theta\cos\beta \end{bmatrix} = \begin{bmatrix} r\sin\theta'\cos\phi' \\ r\sin\theta'\sin\phi' \\ r\cos\theta' \end{bmatrix} \tag{A.4}$$

$$\vec{r}\,' = \mathbf{R}_x(\gamma)\vec{r} = \begin{bmatrix} r\sin\theta\cos\phi \\ r\sin\theta\sin\phi\cos\gamma - r\cos\theta\sin\gamma \\ r\sin\theta\sin\phi\sin\gamma + r\cos\theta\cos\gamma \end{bmatrix} = \begin{bmatrix} r\sin\theta'\cos\phi' \\ r\sin\theta'\sin\phi' \\ r\cos\theta' \end{bmatrix}. \tag{A.5}$$

From (A.3) to (A.5), it is evident that the most convenient rotation to consider from a mathematical point of view is that around z, since it is invariant for θ ($\theta' = \theta$) and involves a simple shift in ϕ ($\phi' = \phi + \alpha$). More complicated transformations $\theta \to \theta'$ and $\phi \to \phi'$ would be required for the other two rotations (A.4) and (A.5). This motivates the choice of the reference system in Fig. A.2, with the z-axis parallel to the slot axis.

When considering the entire array, each radiating element is rotated around the z-axis with the matrix $\mathbf{R}_z(m\alpha)$, with integer $m \in [0, M-1]$:

$$\vec{r}'_m = \mathbf{R}_z(m\alpha)\vec{r} = \begin{bmatrix} r \\ \theta \\ \phi + m\alpha \end{bmatrix} . \tag{A.6}$$

The same rotation is applied to the electric field vector:

$$\vec{E}'_m(\vec{r}) = \mathbf{R}_z(m\alpha)\vec{E}(\vec{r}'_m) = \mathbf{R}_z(m\alpha) \begin{bmatrix} E_x(\vec{r}'_m) \\ E_y(\vec{r}'_m) \\ E_z(\vec{r}'_m) \end{bmatrix} = \begin{bmatrix} E_x(\vec{r}'_m)\cos(m\alpha) - E_y(\vec{r}'_m)\sin(m\alpha) \\ E_x(\vec{r}'_m)\sin(m\alpha) + E_y(\vec{r}'_m)\cos(m\alpha) \\ E_z(\vec{r}'_m) \end{bmatrix} . \tag{A.7}$$

As shown in Fig. A.2(a), the origin of the coordinate system is assumed to be located at the center of the slot feed. Therefore, when constructing the field of the array, an array factor must be considered that accounts for the different positions of the elements on a circle with radius $R = r + h_{\mathrm{br}}$:

$$\vec{E}_{\mathrm{array}}(\vec{r}) = \sum_{m=0}^{M-1} \vec{E}'_m(\vec{r}) e^{jkR\sin\theta\cos(\phi - m\alpha)} .$$

Alternatively, the choice of the reference system in Fig. A.2(b) can be made, where the origin is at the center of the array cylinder. In such a configuration, the rotation around z also accounts for the shift of the elements in a different position. In this case, the far-field pattern of the array becomes

$$\vec{E}_{\mathrm{array}}(\vec{r}) = \sum_{m=0}^{M-1} \vec{E}'_m(\vec{r}) .$$

This Page Intentionally Left Blank

Acronyms

ADLs Artificial Dielectric Layers. 1, 2, 17–19, 27

CST CST Studio Suite. 10, 11

HFSS High Frequency Structure Simulation Software. 2, 5–10, 18, 19, 25, 26, 28, 29, 33, 34, 38, 41, 43

P.M.C Perfect Magnetic Conductor. 29, 30

PCB Printed Circuit Board. 1

PEC Perfect Electrical Conductor. 5, 9

PML Perfectly Matched layer. 5–9, 33, 41, 43

This Page Intentionally Left Blank

Bibliography

[1] M. H. Novak, F. A. Miranda, and J. L. Volakis, "Ultra-wideband phased array for millimeter-wave ISM and 5G bands, realized in PCB," *IEEE Trans. Antennas Propag.*, vol. 66, no. 12, pp. 6930–6938, Dec. 2018.

[2] A. J. Katwijk, A. Neto, G. Toso, and D. Cavallo, "Design of wideband wide-scanning dual-polarized phased array covering simultaneously both the Ku- and the Ka-satcom bands," in *Proc. 14th Eur. Conf. Antennas Propag.*, Copenhagen, Denmark, Mar. 15-20 2020, pp. 1–3.

[3] R. Ozzola, A. Neto, U. Imberg, and D. Cavallo, "Connected slot array with interchangeable ADL radome for sub-8 GHz 5G applications," *IEEE Trans. Antennas Propag.*, vol. 72, no. 1, pp. 992–997, Jan. 2024.

[4] D. H. Schaubert, A. V. Ardenne, C. Craeye, A. O. Boryssenko, and J. G. B. D. Vaate, "The square kilometer array (SKA) antenna," in *Proc. IEEE Int. Symp. Phased Array Systems Tech.*, Boston, MA, USA, Oct. 14-17 2003, pp. 351–358.

[5] E. W. Reid, L. Ortiz-Balbuena, A. Ghadiri, and K. Moez, "A 324-element vivaldi antenna array for radio astronomy instrumentation," *IEEE Trans. Instrum. Meas.*, vol. 61, no. 1, pp. 241–250, Jan. 2012.

[6] S. Kemkemian and M. Nouvel-Fiani, "Toward common radar & EW multifunction active arrays," in *Proc. IEEE Int. Symp. Phased Array Systems Tech.*, Waltham, MA, USA, Oct. 12-15 2010, pp. 777–784.

[7] C. Renard and M. Soiron, "Wideband multifunction airborne antennas," in *Proc. Int. Radar Conf. Surveil. Safer World*, Bordeaux, France, Oct. 12-16 2009, pp. 1–3.

[8] R. Kindt and R. Pickles, "12-to-l bandwidth all-metal vivaldi array element," in *Proc. IEEE Antenna Propag. Soc. Int. Symp.*, North Charleston, SC, USA, Jun. 1-5 2009, pp. 1–4.

[9] M. W. Elsallal and J. C. Mather, "An ultra-thin, decade (10:1) bandwidth, modular BAVA array with low cross-polarization," in *Proc. IEEE Antenna Propag. Soc. Int. Symp.*, Spokane, WA, USA, Jul. 3-8 2011, pp. 1980–1983.

[10] J. J. Lee and S. Livingston, "Wide band bunny-ear radiating element," in *Proc. IEEE Antenna Propag. Soc. Int. Symp.*, vol. 3, Ann Arbor, MI, USA, Jun. 28 - Jul. 2 1993, pp. 1604–1607.

[11] R. W. Kindt and J. T. Logan, "Dual-polarized metal-flare sliced notch antenna array," *IEEE Trans. Antennas Propag.*, vol. 68, no. 4, pp. 2666–2674, Apr. 2020.

[12] J. T. Logan, R. W. Kindt, and M. N. Vouvakis, "A 1.2-12 GHz sliced notch antenna array," *IEEE Trans. Antennas Propag.*, vol. 66, no. 4, pp. 1818–1826, Apr. 2018.

[13] H. A. Wheeler, "Simple relations derived from a phased-array antenna made of an infinite current sheet," *IEEE Trans. Antennas Propag.*, vol. 13, no. 7, pp. 506–514, Jul. 1965.

[14] J. P. Doane, K. Sertel, and J. L. Volakis, "A wideband, wide scanning tightly coupled dipole array with integrated balun (TCDA-IB)," *IEEE Trans. Antennas Propag.*, vol. 61, no. 9, pp. 4538–4548, Sep. 2013.

[15] H. Zhang, S. Yang, Y. Chen, J. Guo, and Z. Nie, "Wideband dual-polarized linear array of tightly coupled elements," *IEEE Trans. Antennas Propag.*, vol. 66, no. 1, pp. 476–480, Jan. 2018.

[16] J. T. Logan, R. W. Kindt, M. Y. Lee, and M. N. Vouvakis, "A new class of planar ultrawideband modular antenna arrays with improved bandwidth," *IEEE Trans. Antennas Propag.*, vol. 66, no. 2, pp. 692–701, Feb. 2018.

[17] E. Yetisir, N. Ghalichechian, and J. L. Volakis, "Ultrawideband array with 70° scanning using FSS superstrate," *IEEE Trans. Antennas Propag.*, vol. 64, no. 10, pp. 4256–4265, Oct. 2016.

[18] D. Cavallo, "Recent advances on wideband wide scanning connected slot arrays," in *IEEE Int. Symp. Phased Array Systems Tech.*, Waltham, MA, USA, Oct. 11-14 2022, pp. 1–3.

[19] ——, "Connected slot antennas for wideband wide-scan phased arrays," in *IEEE Int. Symp. Phased Array Systems Tech.*, Boston, MA, USA, Oct. 15-18 2024, pp. 1–3.

[20] L. Josefsson and P. Persson, *Conformal Array Antenna Theory and Design*. Hoboken, NJ, USA: John Wiley and Sons, Inc., 2006.

[21] C. Fulton, J. L. Salazar, Y. Zhang, G. Zhang, R. Kelly, J. Meier, M. McCord, D. Schmidt, A. D. Byrd, L. M. Bhowmik, S. Karimkashi, D. S. Zrnic, R. J. Doviak, A. Zahrai, M. Yeary, and R. D. Palmer, "Cylindrical polarimetric phased array radar: Beamforming and calibration for weather applications," *IEEE Trans. Geosci. Remote Sens.*, vol. 55, no. 5, pp. 2827–2841, May 2017.

[22] J. Yang, X. Lu, Z. Dai, W. Yu, and K. Tan, "A cylindrical phased array radar system for UAV detection," in *Proc. IEEE 6th Int. Conf. Intelligent Computing Signal Processing*, Xi'an, China, Apr. 9-11 2021, pp. 894–898.

[23] J. C. Sureac and A. Hessel, "Element pattern for circular arrays of axial slits on large conducting cylinders," *IEEE Trans. Antennas Propag.*, vol. 17, no. 6, pp. 799–803, Nov. 1969.

[24] G. V. Borgiotti and Q. Balzano, "Mutual coupling analysis of a conformal array of elements on a cylindrical surface," *IEEE Trans. Antennas Propag.*, vol. 18, no. 1, pp. 55–63, Jan. 1970.

[25] J. C. Herper, A. Hessel, and B. Tomasic, "Element pattern of an axial dipole in a cylindrical phased array, part I: Theory," *IEEE Trans. Antennas Propag.*, vol. 33, no. 3, pp. 259–272, Mar. 1985.

[26] ——, "Element pattern of an axial dipole in a cylindrical phased array, part II: Element design and experiments," *IEEE Trans. Antennas Propag.*, vol. 33, no. 3, pp. 273–278, Mar. 1985.

[27] B. Tomasic and N. Herscovici, "Analysis of cylindrical array of infinitely-long slots fed by connected dipoles," in *Proc. IEEE Antenna Propag. Soc. Int. Symp.*, North Charleston, SC, USA, Jun. 1-5 2009, pp. 1–4.

[28] J. T. Logan, W. M. Dorsey, and J. A. Valenzi, "Modular all-metal ultrawideband cylindrical array for multifunction operation," *IEEE Trans. Antennas Propag.*, vol. 70, no. 10, pp. 9175–9183, Oct. 2022.

[29] Y. Gao, D. Wu, and Q. Wu, "Analysis of conformal antenna arrays using cylindrical periodic Green's function and RWG basis function," *IEEE Trans. Antennas Propag.*, vol. 72, no. 2, pp. 1385–1396, Feb. 2024.

[30] Ansys HFSS, ver. 20, Ansys, Inc., Canonsburg, PA, USA. [Online]. Available: https://www.ansys.com/

[31] A.K. Bhattacharyya, *Phased Array Antennas: Floquet Analysis, Synthesis, BFNs and Active Array Systems*. Hoboken, NJ, USA: John Wiley & Sons, 2006.

[32] CST Studio Suite, ver. 20, Dassault Systèmes Simulia Corp. , Johnston, RI, USA. [Online]. Available: https://www.3ds.com/products/simulia/cst-studio-suite/

[33] R. Ozzola, D. Cavallo, and A. Neto, "On the relation between beam coupling and feed coupling in wideband antenna arrays," *IEEE Trans. Antennas Propag.*, vol. 70, no. 6, pp. 260 – 267, June 2021.

[34] D. Cohen and R. Shavit, "Bi-anisotropic metamaterials effective constitutive parameters extraction using oblique incidence s-parameters method," *IEEE Trans. Antennas Propag.*, vol. 63, no. 5, pp. 2071–2078, May 2015.

[35] D. Cavallo and C. Felita, "Analytical formulas for artificial dielectrics with nonaligned layers," *IEEE Trans. Antennas Propag.*, vol. 65, no. 10, pp. 5303–5311, Oct. 2017.

[36] D. M. Pozar, *Microwave engineering; 4th ed.* Hoboken, NJ, USA: John Wiley & Sons, Inc., 2012.

[37] C. M. Coco Martin, W. Hu, and D. Cavallo, "Design of wideband flat artificial dielectric lenses at mmwave frequencies," *IEEE Trans. Antennas Propag.*, vol. 72, no. 2, pp. 1418–1428, Feb. 2024.

[38] W. Hu, C. M. Coco Martin, and D. Cavallo, "Design formulas for flat gradient index lenses with planar or spherical output wavefront," *IEEE Trans. Antennas Propag.*, vol. 72, no. 3, pp. 2555–2563, Mar. 2024.

[39] R. G. Tapia Barroso, A. Neto, and D. Cavallo, "Study of finite edge effects in compact ultra-wide-band connected arrays," in *18th Eur. Conf. Antennas Propag.*, Glasgow, Scotland, Mar. 17-22 2024.

[40] A. Ishimaru, R. Coe, G. Miller, and W. Geren, "Finite periodic structure approach to large scanning array problems," *IEEE Trans. Antennas Propag.*, vol. 33, no. 11, pp. 1213–1220, Nov. 1985.